1   Structure of a proton-powered molecular motor that drives protein transport and gliding motility

2   Rory Hennell James[1,2*], Justin C. Deme[1,2,3*], Andreas Kjær[2], Felicity Alcock[2,4], Augustinas Silale[2,4],

3   Frédéric Lauber[2], Ben C. Berks[2†], and Susan M. Lea[1,3†]

4

5

6   [1] Sir William Dunn School of Pathology, University of Oxford, South Parks Road, Oxford OX1 3RE,

7   United Kingdom.

8   [2] Department of Biochemistry, University of Oxford, South Parks Road, Oxford OX1 3QU, United

9   Kingdom.

10   [3] The Central Oxford Structural Molecular Imaging Centre (COSMIC), University of Oxford, South Parks

11   Road, Oxford OX1 3RQ, United Kingdom.

12   4. Current address: CBCB, Newcastle Univeristy, NE17RU UK

13   * These authors contributed equally to this work.

14   † To whom correspondence should be addressed. S.M.Lea (susan.lea@path.ox.ac.uk); B.C.Berks

15   (ben.berks@bioch.ox.ac.uk).

16   **Summary**

17   Ion-driven motors are rare in biology. The archetypes of the three classes identified to date are ATP

18   synthase, the bacterial flagellar motor, and a proton-driven motor that powers gliding motility and

19   protein secretion in *Bacteroidetes* bacteria. Whilst the molecular mechanism of ATP synthase is now

20   well understood, structural information is lacking for the other two classes of motor. Here we present

21   the structure of the *Bacteroidetes* gliding motility motor determined by cryo-electron microscopy. The

22   motor is an asymmetric inner membrane protein complex in which the single transmembrane helices

23   of two periplasm-spanning GldM proteins are positioned within a ring of five GldL proteins. Combining

24   mutagenesis and single-molecule tracking, we identify protonatable amino acid residues within the

25   transmembrane domain of the complex that are important for motor function. Our data imply a

26   mechanism in which proton flow leads the periplasm-spanning GldM dimer to rotate with respect to

27   the intra-membrane GldL ring to drive processes at the bacterial outer membrane. This work provides

28   a molecular basis for understanding how the gliding motility motor is able to transduce the energy of

29   the inner membrane protonmotive force across the bacterial cell envelope.

30

31 **Main**

32   The use of transmembrane ion-motive electrochemical gradients to drive biochemical processes is

33   one of the fundamental features of cellular life[1]. Most commonly ion movement down the

34   electrochemical gradient is coupled to transport processes or signalling. However, ion gradients can

35   also be exploited to power the mechanical motions of membrane-associated molecular motors. Three

36   classes of ion-driven machines are known. In ATP synthases the ion-motive gradient drives a rotary

37   movement that results in the energy-requiring release of ATP from the catalytic sites of the enzyme[2,3].

38   A second class of ion-driven mechanical motor is associated with the bacterial flagellum that drives

39   swimming motility. In this system, ion flow through stator units linked to the cell wall results in a

40   mechanical force on the base of the flagellum that causes the flagellum to rotate[4,5](Deme et al.,

41   companion paper). Additional members of the flagellar stator family include the periplasm-spanning

42   Ton and Tol complexes which mechanically drive processes at the outer membrane (OM) of Gram-

43   negative bacteria using the inner membrane (IM) protonmotive force (PMF)[6,7](Deme et al. companion

44   paper). The third type of ion driven motor is found in bacteria of the phylum *Bacteroidetes.* The motor

45   in these bacteria powers rapid gliding motility across solid surfaces[8] using the PMF across the IM as

46   the energy source [9-11]. The gliding motility motor generates a rotary motion at the cell surface [11] that

47   results in a helical flow of surface adhesins [9,12,13], possibly by driving a mobile track to which the

48   adhesins are attached [14].

49   Work with the model gliding bacterium *Flavobacterium johnsoniae* strongly suggests that the two

50   conserved IM proteins GldL and GldM form the PMF-transducing gliding motility motor[15](Fig. 1a).

51   Neither of these proteins has detectable sequence similarity to the components of the other classes

52   of ion-driven motors. GldL is composed of two predicted transmembrane helices (TMH) followed by a

53   long cytoplasmic tail [16]. GldM is mainly periplasmic and anchored to the IM by a N-terminal TMH [16]. A

54   recent structure of the periplasmic portion of GldM reveals that it contains four folded domains which

55   assemble as a homodimeric rod that is long enough (180Å) to span the periplasm[17]. The distal end of

56   GldM contacts a large ring structure at the OM, composed of the proteins GldK and GldN, which is

57   thought to link the GldLM motor to the gliding apparatus [17,18].

58   In addition to their role in gliding motility, GldL and GldM have been found to be essential for

59   protein export across the OM by the *Bacteroidetes*-specific Type IX secretion system (T9SS) [15,19]. Thus,

60   the gliding motility motor is likely to also be involved in energizing protein movement through the

61   T9SS apparatus[20-22]. Notably, GldLM homologues are still required for protein secretion in non-gliding

62   *Bacteroidetes* species with a T9SS, such as *Porphyromonas gingivalis*, the causative agent of severe

63   periodontal disease[19,22]. The involvement of GldLM in the T9SS leads to the prediction that Type 9

64   protein transport should be energized by the PMF. In agreement with this hypothesis, we find that

65   protein export by the T9SS is PMF-dependent (Extended Data Fig. 1).

66

67   **The GldLM is an inherently asymmetric 5:2 subunit complex**

68   The intact GldLM motor complex proved unsuitable for high resolution structure determination by

69   cryo-electron microscopy because the anisotropic shape of the molecule led to a poor distribution of

70   views. However, imaging a *F. johnsoniae* GldLM complex in which the GldM protein has been C-

71   terminally truncated after the first folded periplasmic domain (hereafter referred to as GldLM')

72   allowed the calculation of an EM volume at 3.9 Å resolution and *de novo* building of a full atomic

73   model (Fig. 1b-e, Extended Data Table 1, Extended Data Fig. 2-3). The transmembrane domain of the

74   complex is fully defined in the resulting model (Fig. 1c-e). GldL is ordered between residue 3 and 62

75   (Fig 1b) with 153 residues of the cytoplasmic C-terminus not resolved in the current volume. The

76   ordered portion of GldL forms a pair of TMHs arranged at ~25° to the membrane normal with a well-

77   structured loop joining them on the periplasmic face of the membrane (Fig. 1b). Almost the entirety

78   of the truncated GldM construct could be modelled (residue 7 to 225, Fig. 1b). The single-pass TMH is

79   resolved and is topped by the periplasmically-located helical domain (0.7Å RMSD to the X-ray

80   structure) (Fig. 1b). The overall complex is formed from five copies of GldL and two copies of GldM

81   (Fig. 1d,e) with the GldL TMH pairs forming a distorted pentameric cage enclosing the two copies of

82   the GldM TMH. Consequently, the predicted TMH of GldM is found entirely within a proteinaceous

83   environment with no exposure to the lipid bilayer (Fig. 1e). The periplasmic domains of the GldM

84   subunits pack against the top of the ring of GldL TMHs (Fig. 1d,e).

85   The overall structure of the GldLM' complex is strikingly asymmetric both in the plane of the

86   membrane, due to the stoichiometry mismatch of the two types of subunit within the TM helix bundle,

87   and because the periplasmic domains of GldM adopt different tilts relative to the top of their TMHs

88   (Fig. 1d,e). The result is that both within the membrane domain, and at the periplasmic subunit

89   interface, each of the five copies of GldL make different contacts to GldM (Extended Data Table 2).

90   Notably, only a single conformation of the GldLM' complex is seen in our current data. Within the

91   GldLM' complex the TMHs are closely packed (Fig. 1e), implying that conformational change in the

92   TMH of one subunit of the complex will only be possible if there are concerted conformational changes

93   in the other subunits. As expected, the surfaces buried between the subunits of the GldLM' complex

94   are highly conserved and the exposed surfaces highly variable (Extended Data Fig. 4).

95

96

97

98   **Identification of functionally important residues within the transmembrane domain of the GldLM**

99   **complex**

100   The membrane domain of a proton-driven motor is anticipated to contain protonatable amino

101   acid side chains that function to couple the transmembrane proton flow to the conformational

102   changes required to do mechanical work. We, therefore, used site directed amino acid substitutions

103   to test the functional importance of polar residues within the GldLM transmembrane helical bundle.

104   No GldM protein was detected for variants with non-conservative substitutions of $GldM_{R9}$, probably

105   because this residue functions as a topogenic signal for membrane protein insertion [23](Extended Data

106   Fig. 5). The $GldL_{E49D}$ variant also had reduced levels of protein expression, but this change is insufficient

107   to account for the complete null phenotype of this variant (below).

108   Gliding motility was assessed by spreading behaviour on agar plates (Fig. 2a) and by microscopic

109   examination of gliding on glass (Extended Data Table 3 and Supplementary Video 1). T9SS activity in

110   the mutant strains was assessed through monitoring secreted chitinase activity (Fig. 2b). The effects

111   of the substitutions on gliding were more severe than on T9SS function, suggesting that motility

112   requires a higher level of motor function. The gliding phenotypes of the GldLM variants will reflect not

113   only the direct effect of the substitutions on adhesin movement but also their influence on the T9SS-

114   dependent export of the adhesins[15]. To assess the effects of the motor protein substitutions on

115   adhesin flow independent of T9SS function, we tracked the movements of individual fluorophore-

116   labelled adhesin molecules. In mutants that showed impaired gliding, but which retained the ability

117   to export adhesins to the cell surface, the adhesin molecules were still observed to move in helical

118   patterns. However, the average speed of adhesin movement was dramatically slower than in the

119   parental strain (Fig. 2c,d and Supplementary Videos 2-7). Thus, the GldLM substitutions in these

120   strains directly affect the mechanical force driving adhesin movement, as expected of defects in the

121   gliding motility motor.

122   The results of our amino acid substitution experiments (Extended Data Table 3) show that

123   functionally important protonatable amino acids are clustered both within the membrane core of the

124   GldLM complex and at the periplasmic GldL/GldM interface (Fig. 2e). The tight packing of the

125   transmembrane helix bundle (Fig. 1e) seen in the structure provides no route for proton movement

126   between these two layers of residues. This implies that the motor cycle must include a conformational

127   change to open an aqueous channel between these regions at one point in the ring.

128   Within the membrane core the invariant residues $GldL_{E49}$ and $GldM_{Y17}$ and the highly conserved

129   residues $GldL_{Y13}$ and $GldM_{R9}$ are important for motor function. The symmetry mis-match in the GldLM'

130   complex means that within each chain these residues are in a different environment. Thus, in one

131   GldM copy $GldM_{R9}$ (chain B; coloured grey in the figures) is positioned to form a salt bridge with $GldL_{E49}$

132   (chain E, coloured salmon in the figures), whilst $GldM_{Y17}$ (chain A, coloured white in the figures) and

133    $GldL_{Y13}$ (chain E) bracket this pair of residues (Fig 3a). By contrast, $GldM_{R9}$ in the other copy of GldM

134   (chain A) is rotated away from $GldL_{E49}$ on the nearest GldL subunit and so these two residues are no

135   longer positioned to interact. The substitution data show that protonation of the $GldL_{Y13}$ and $GldM_{Y17}$

136   side chains is important for their function, as expected if these residues are involved in transducing

137   transmembrane proton movements to mechanical work. However, the substitution data also show

138   the importance of the aromatic nature of $GldL_{Y13}$ and $GldM_{Y17}$, suggesting that these residues are

139   additionally involved in mechanistically important packing interactions.

140

141   **Structural asymmetry in the GldLM complex**

142   An overlay of the two GldM' subunits shows that the cytoplasmic end of the TMH must be bent in

143   order for $GldM_{R9}$ to ion pair with $GldL_{E49}$ (Fig. 3b). In this ion-paired copy of GldM the angle between

144   the TMH and the periplasmic domain is less acute than in the other GldM chain, and so the periplasmic

145   domain is less tilted relative to the GldL ring (Figs. 2e and 3c). Indeed, it is the periplasmic domain of

146   the GldM subunit that is not participating in the ion pair that tilts sufficiently to make extensive

147   interactions with the top of the ion-paired GldL subunit (Fig. 2e and 3b,c).

148   An overlay of the five copies of the GldL protein found in the GldLM' complex reveals that the helix

149   in which $GldL_{E49}$ is positioned to ion pair with $GldM_{R9}$ is shifted compared to the equivalent helix in the

150   other copies of GldL (Fig. 3c). This helix movement is accompanied by a reorientation of $GldL_{Y13}$ located

151   on the second TMH of the same chain and a remodelling of the periplasmic loop that is packed against

152 the GldM periplasmic domain (Fig. 3c). These changes in GldL conformation are likely linked to

153 conformational differences between the two copies of GldM and imply that mechanical forces exerted

154 on the GldM subunits within the membrane are reinforced by interactions between the GldM

155 periplasmic domains and the top of the GldL ring. Notably, substitution of two invariant residues

156 ($GldL_{K17}$ and $GldL_{H20}$) within the GldL periplasmic loop that appear to mediate interactions with the

157 GldM periplasmic domain significantly impair gliding motility (Figs. 2a,c,d and 3c).

158 Taken together these observations show that the presence or absence of the $GldM_{R9}$ – $GldL_{E49}$ ion

159 pair in the two copies of the GldM protein is linked to conformational differences between the

160 proteins. This suggests a simple model of reciprocal conformational change between the two GldM

161 copies to produce mechanical force in the periplasm. In this model the $GldM_{R9}$ – $GldL_{E49}$ ion pair

162 involving one GldM subunit is broken by protonation of $GldL_{E49}$ by an incoming proton from the

163 periplasmic side of the membrane, subsequent to which $GldM_{R9}$ on the other GldM subunit forms an

164 equivalent ion pair through ejection of a proton from $GldL_{E49}$ on the nearest GldL molecule. $GldM_{Y17}$

165 and $GldL_{Y13}$ are well-positioned to act as the proton donor and acceptor, respectively, to the $GldM_{R9}$ –

166 $GldL_{E49}$ ion pair. In this context, the movement of the $GldL_{Y13}$ side chain away from the ion pair in the

167 salt-bridged copy of GldL might be a mechanism to prevent the immediate short-circuiting transfer of

168 the proton to the cytoplasm following protonation of the ion pair. Co-operative movements of the

169 two GldM proteins will be reinforced by the fact that it is the GldM subunit that is not involved in the

170 ion pair that both provides the apparent proton donor to the ion pair (through $GldM_{Y17}$) and that

171 possesses the periplasmic domain that forms intimate contacts with the periplasmic loops of the GldL

172 subunit involved in the ion pair.

173

174 **Orientation of the GldM periplasmic domains**

175 An overlay of the first periplasmic domains of GldM in our cryoEM structure with the equivalent

176 domains in the previously reported crystal structures of the dimeric, isolated, GldM periplasmic

177 region[17] demonstrates that the two copies of the domain are splayed apart in the cryoEM structure

178 compared to the earlier crystal structure (Fig. 4a). We were concerned that this difference between

179 the two structures might have arisen due to our truncation of the periplasmic region of GldM, even

180 though neither co-variance nor conservation suggest a strong dimerization interface between these

181 first periplasmic domains (Extended Data Fig. 4) and the isolated domain from the *P. gingivalis*

182 homologue crystallises as a monomer[17]. To resolve this issue we turned to lower resolution cryoEM

183 volumes derived from images of full length GldLM complexes. Data from the *P. gingivalis* GldLM

184 homologue PorLM were of sufficient quality to allow location of the two TMH helices of PorM enabling

185 us to position the atomic model for *F. johnsoniae* GldLM' within the lower resolution *P. gingivalis*

186 PorLM volume (Fig 4b,c). Interpretation of the lower resolution volume in this way demonstrates that

187 even in the context of the full length GldM homologue the GldM first periplasmic domains are splayed

188 with an acute (and different between the two copies) angle between the first and second domains

189 (Fig 4c). Density for the second periplasmic domain is also visible in the volume and is compatible with

190 the strand-swapped dimeric arrangement of this domain seen in the crystal lattice despite the

191 separation of the first domain. The splaying of GldM is likely driven by packing of the first periplasmic

192 domains onto the top of the GldL transmembrane domains and packing of the N-terminal helices

193 within the GldL cage. The need to anneal the two GldM chains above this domain may explain the

194 unusual strand-swapped dimer that forms the next (second) periplasmic domain. More distal domains

195 were only present in the volume at very low contour levels presumably due both to their distance

196 from the centre of the alignment and to some conformational variability of the entire periplasmic

197 portion with respect to the transmembrane region. Nevertheless, no further large deviations from a

198 linear conformation are seen for the distal domains. Combining our structural information with the

199 earlier crystallographic data generates a composite model for the GldLM complex in which the rod-

200   like periplasmic region of GldM projects into the periplasm at an appreciable angle away from the

201   membrane normal (Fig. 4d).

202

203   **Discussion**

204   The GldLM' structure reveals an asymmetric complex bedded in the inner membrane. The lack of

205   shared symmetry between the components of the GldLM' complex, together with the caging of GldM

206   within GldL, suggests that rotation of GldM within the GldL ring is the most likely mechanical

207   movement produced by the motor. This type of motion would be consistent with the observation

208   that the gliding motility system is able to generate rotary motion at the cell surface[11]. In order for the

209   GldLM motor to drive processes at the OM through rotation of the distal end of GldM, GldL must

210   remain stationary in the IM to act as a stator to the rotating GldM protein. GldL cannot be immobilized

211   by binding to the cell wall since GldM covers the parts of GldL that are exposed at the periplasmic side

212   of the membrane. Instead, it is likely that GldL is held in position through interactions between the

213   currently unvisualized cytoplasmic tail and a static cytoplasmic structure. Sequential morphing of the

214   structure between the GldL conformational states was used to produce an animation that indicates

215   the approximate molecular changes that would occur in the GldLM complex on rotation of the GldM

216   periplasmic domain (Supplementary Video 8).

217   The arrangement of the ten GldL TMHs around two central GldM TMHs is reminiscent of the

218   structural organization of the transmembrane core of the flagellar MotAB stator complex (reported in

219   our companion paper (Deme et al. companion paper)) and the related ExbBD complex of the Ton

220   system [6](Deme et al. companion paper) even though the mobile and stationary components of the

221   GldLM motor are reversed relative to MotAB. This organizational similarity is particularly remarkable

222   given the lack of detectable sequence similarity between GldLM and the subunits of the other motor

223   complexes. The implications of this protein architecture being shared between bacterial ion-driven

224   motors are discussed in the companion paper (Deme et al., companion paper).

225

226

Acknowledgements

240

Author contributions

R.H.J carried out all genetic and biochemical work except as credited otherwise. J.C.D. and S.M.L. collected EM data and determined the structure. A.K. developed and carried out the SprB tracking experiments including strain construction. F.A. carried out the pulse chase analysis of protein export, A.S. assayed cellular ATP levels, F.L. constructed the Δ*gldL* strain and produced the GldL and GldM antibodies. B.C.B. and S.M.L. conceived the project. All authors interpreted data and wrote the manuscript.

248

249   **Figure legends**
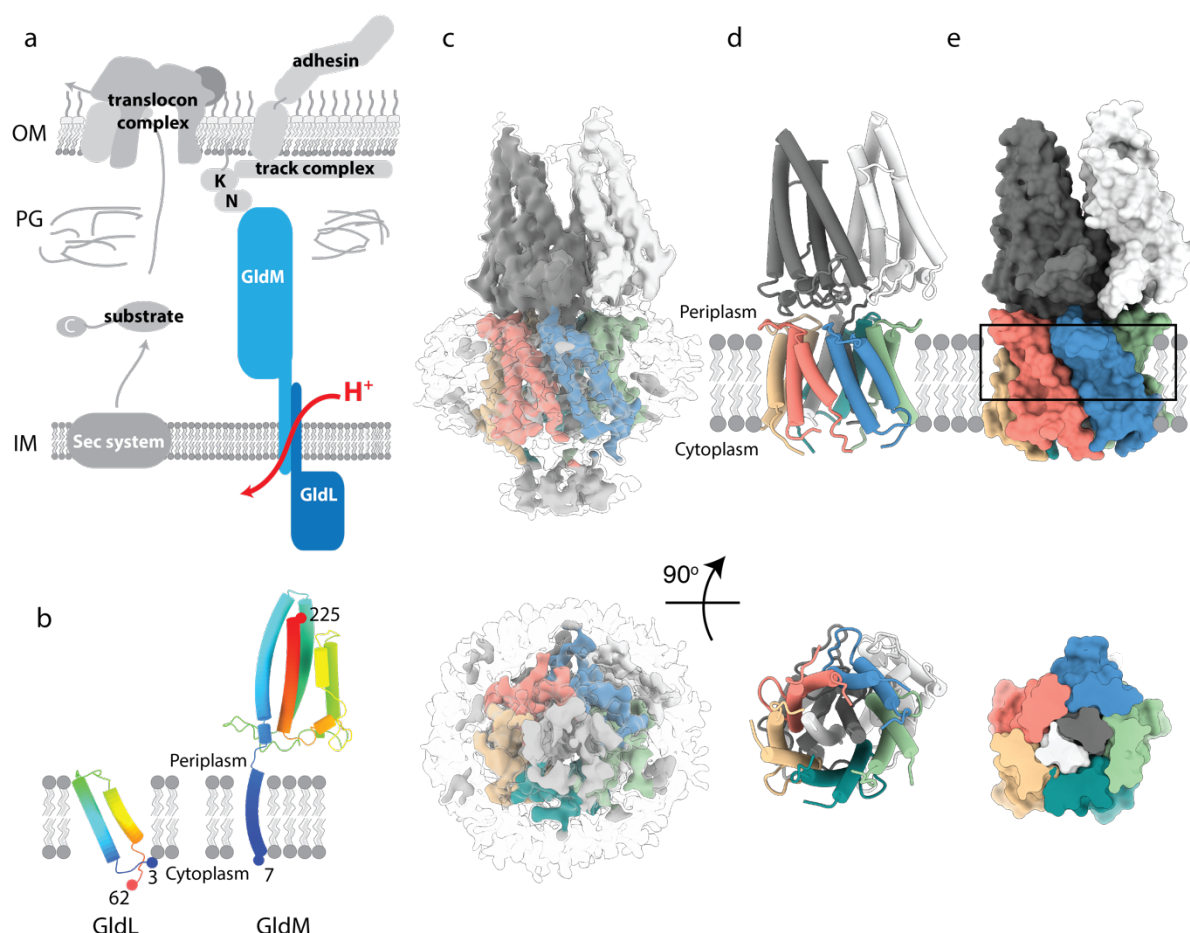
250

251

252   **Fig. 1 | Structure of the *F. johnsoniae* GldLM' complex. a**, Schematic showing the relationship of the
253   GldLM complex to the major components of the T9SS (left) and gliding motility (right) systems. OM,
254   outer membrane; IM inner membrane; PG peptidoglycan. **b**, Structures of individual GldL and GldM
255   subunits extracted from the complex. **c**, 3D cryo-EM reconstruction of the LMNG-solubilised GldLM'
256   complex at high (coloured by protein chain) and low (semi-transparent grey) contours. The detergent
257   micelle is seen at the low contour level and is used to estimate the location of the membrane bilayer
258   shown in **d,e**. **d,e** Cartoon and space-filling representations of the GldLM' complex. The GldL subunits
259   are coloured salmon, blue, green, teal, and yellow, and the GldM subunits are coloured white and dark
260   grey. In **e** the lower panel shows a slab through the region indicated by the box in the upper panel. In
261   **c-e** the lower panels show the complex viewed from the cytoplasm.

262
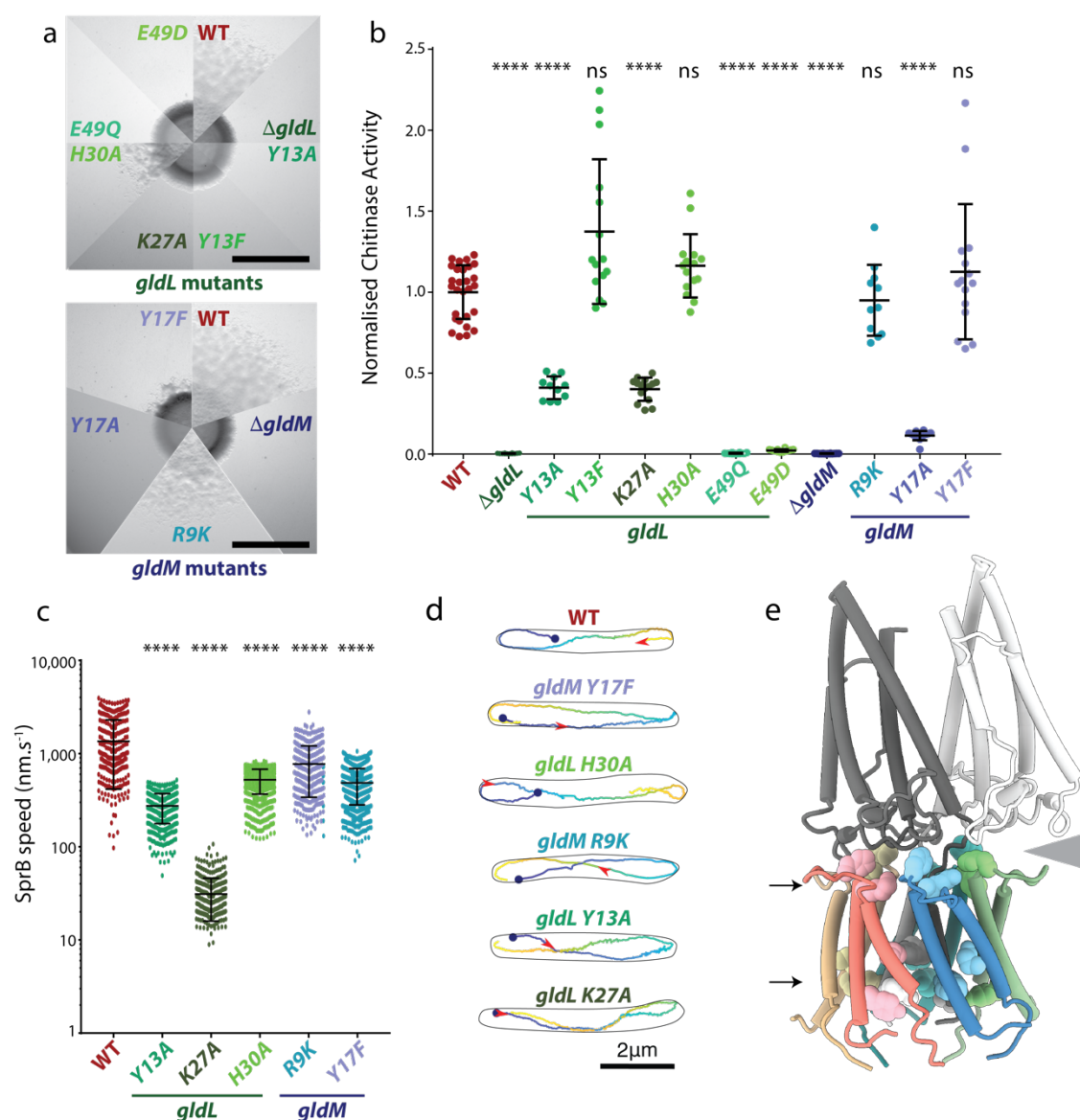
263

264

Fig. 2 | Functional analysis of protonatable residues in the transmembrane domain of GldLM. a-d, Phenotypic comparisons between wild type (WT) cells and *gldLM* single codon mutants. **a,** Gliding motility assessed by spreading on agar plates. **b,** Extracellular levels of the T9SS-secreted enzyme chitinase. Error bars show 1 standard deviation. Significance of differences relative to WT were assessed with Dunn's multiple comparisons test (non normally distributed) or Dunnet's multiple comparison test. **** = p < 0.0001, ns = not significant. At least 3 technical replicates of at least 3 biological repeats were performed for each strain. **c-d,** Cell surface movement of single fluorophore-labelled SprB adhesin molecules. **c,** Plot showing the speed of helically moving adhesins in a WT (321 tracks), *gldL_{Y13A}* (499 tracks), *gldL_{K27A}* (369 tracks), *gldL_{H30A}* (2,259 tracks), *gldM_{R9K}* (429 tracks) or *gldM_{Y17F}* (1519 tracks) background. For each strain the tracks are pooled data from the analysis of 3 independent cultures. Error bars show 1 standard deviation. Significance of differences relative to the WT was assessed with Dunn's multiple comparisons test. **** = p < 0.0001. **d,** Examples of adhesin helical tracks extracted from Supplementary Videos 2-7 and coloured from blue (start) to yellow (end).

278   The red arrowhead marks the position along the track that the adhesin has reached at 3.5s after the
279   start point (blue dot). **e**, Protonatable residues in GldLM that exhibit reduced function when
280   substituted. The residues are show in space-filling representation on a cartoon model of GldLM' and
281   fall in two bands (indicated with arrows) located at the periplasmic GldL-GldM interface and close to
282   the cytoplasmic end of the TMH bundle. The grey wedge indicates the space between one of the GldM
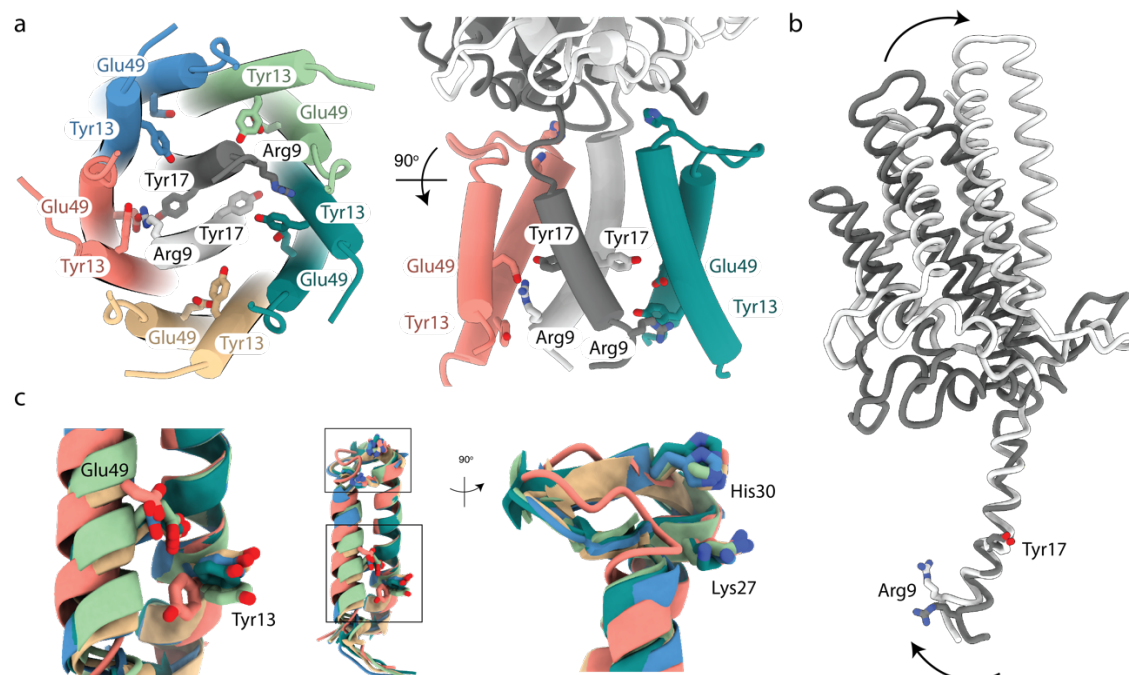283   subunits and the top of the GldL ring.
284

285

286

Fig. 3 | The structural asymmetry of the GldLM' complex leads to important differences in residue environments between chains. The side chains of functionally important resides are shown in stick representation with oxygen atoms red and nitrogen atoms blue. Proteins chains are coloured as in Fig. 1 c-e. **a**, The side chains of functionally important resides near the cytoplasmic end of the TMH bundle. For clarity, only two GldL subunits are shown in the right hand view. **b**, Overlay of the two copies of GldM by superposition of the TMH. **c**, Superposition of the five copies of GldL by overlaying TMH2. The boxes in the central panel indicating the positions of the two regions magnified on either side.
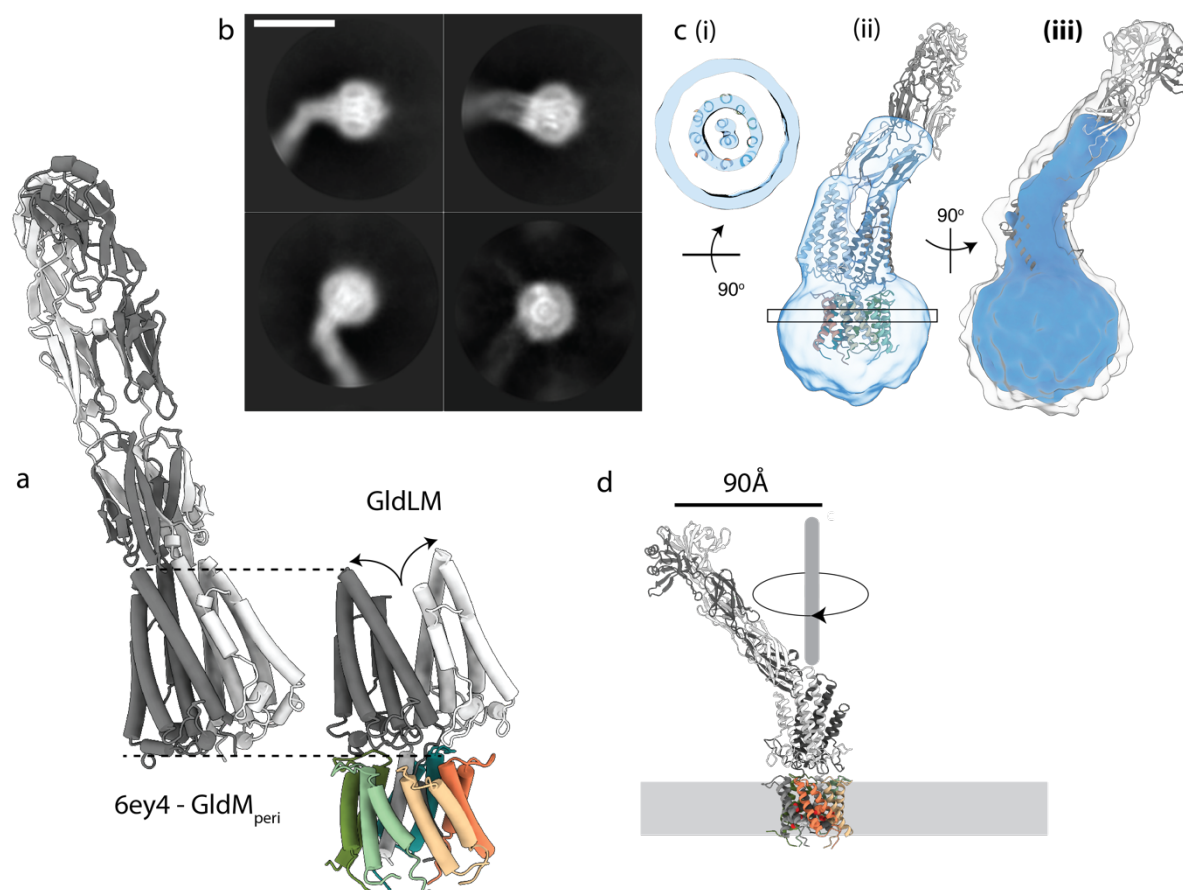
294

Fig. 4 | Structure of the full length motor complex. a, Comparison of the crystal structure of the periplasmic domains of GldM (PDB 6ey4, GldM$_{peri}$) with the cryoEM structure of the periplasmically truncated GldLM' complex. The structures are displayed with the first periplasmic domain of the dark grey GldM chain aligned (dotted lines) and demonstrate the splaying (curved arrows) of the GldM chains in the context of the truncated complex. **b**, Representative 2D classes from micrographs of the full-length *P. gingivalis* motor (PorLM) showing detail in the transmembrane region (all 4 panels), a large bend between the first two periplasmic domains of PorM (left panels), and splaying of the first periplasmic domains of the two copies of PorM (upper right panel). Scale bar 100 Å. **c**, Different views of the *P. gingivalis* motor 3D cryo-EM volume at a high (blue) and low (white) contour level. (**i**) The PorM TMHs can be resolved allowing confident placement of the *F. johnsoniae* GldLM' model in the volume. (**ii**) Splaying of the PorM first periplasmic domain pair is seen as in the *F. johnsoniae* GldLM' complex. (**jjj**) The extension to the volume seen at a low contour level matches well to the length and shape of the dimeric GldM periplasmic domains 2-4 seen in the crystal structure. **d**, Cartoon to demonstrate how the bend between periplasmic domains 1 and 2 would allow the tip of a rotating GldM/PorM to define a large track at the outer-membrane.

Methods

313   No statistical methods were used to predetermine sample size. The experiments were not randomized

314   and the investigators were not blinded to allocation during experiments and outcome assessment.

315

Bacterial strains and growth conditions

317   All strains and plasmids used in this work are listed in Extended Data Tables 4 and 5. *F. johnsoniae*

318   was routinely grown in Casitone Yeast Extract (CYE) medium[24] at 30 °C with shaking. To assess motility

319   on glass and for chitinase secretion measurements cells were grown in Motility Medium[25] (MM). PY2

320   medium[26] was used to assess motility on agar plates. *E. coli* cells were routinely grown in Luria Bertani

321   (LB) medium at 37 °C with shaking. When required, antibiotics were added at the following

322   concentrations: erythromycin, 100 µg ml^{-1}; spectinomycin, 100 µg ml^{-1}; ampicillin, 100 µg ml^{-1};

323   kanamycin, 30 µg ml^{-1}.

324

Genetic constructs

326   All primers used in this work are described in Supplementary Data Table 1. All plasmid constructs

327   were verified by sequencing.

328   A vector directing the co-expression of *F. johnsoniae* GldL and C-terminally truncated GldM was

329   produced as follows. The chromosomal region encoding GldL and the first 225 amino acids of GldM

330   was amplified using primers RHJ164 and RHJ165. The plasmid pT12[27] was linearized by amplification

331   with primers RHJ162 and RHJ163. The two fragments were assembled by Gibson cloning to yield

332   plasmid pRHJ007. A vector for expression of *F. johnsoniae* GldL and the first 232 amino acids of GldM

333   was produced similarly, using primer pair RHJ166 & RHJ167 to create pRHJ008.

334   A vector directing the co-expression of *P. gingivalis* ATCC 33277 PorL and PorM in *E. coli* was

335   produced as follows. pWALDO-sfGFP[28] was digested with BamHI and HindIII and the resulting

336   fragment coding for the TEV cleavage site, superfolder GFP, and a His$_8$ tag was ligated into the

337   corresponding sites in the first multiple cloning site of pCDFDuet-1 (Novagen), yielding plasmid

338   pRHJ001. A C-terminal Twin-Strep tag-coding sequence was added to the second multi-cloning site of

339   pRHJ001 by Q5 site-directed mutagenesis (New England Biolabs) using primers RHJ025 and RHJ026,

340   giving plasmid pRHJ002. The NcoI site in the superfolder GFP-coding sequence was removed by

341   QuikChange mutagenesis (Agilent) using primers RHJ046 and RHJ047, yielding plasmid pRHJ003.

342   pRHJ003 was digested with NcoI and XhoI and the resulting fragment ligated into the corresponding

343   sites of pETDuet-1 to give pRHJ004. *P. gingivalis porL* was amplified from genomic DNA with primers

344   RHJ051 and RHJ052. The resulting 0.9 kb fragment was inserted between the NcoI and BamHI sites of

345   pRHJ004 to give pRHJ005. *P. gingivalis porM* was amplified with primers RHJ057 and RHJ058. The

346   resulting 1.6 kb fragment was inserted between the NdeI and KpnI sites of pRHJ005 to give pRHJ006.

347   A suicide vector to produce an in-frame unmarked deletion of *F. johnsoniae gldL* was produced as

348   follows. A 2.6 kbp region corresponding to the first 36 bp of *gldL* together with the directly upstream

349   region was amplified with primers FL309 and FL310. A 2.5 kbp region corresponding to the final 36 bp

350   of *gldL* together with the directly downstream region was amplified with primers FL311 and FL312.

351   The vector pYT313[29] was linearized by amplification with primers FL313 and FL314. These three

352   fragments were then assembled by Gibson cloning to give plasmid pFL89.

353   A suicide vector to produce an in-frame unmarked deletion of *F. johnsoniae gldM* was produced as

354   follows. A 2.7 kb region corresponding to the first 31 bp of *gldM* together with the directly upstream

355   region was amplified with primers RHJ148 and RHJ160. A 2.5 kb region corresponding to the final 38

356   bp of *gldM* together with the directly downstream region was amplified using primers RHJ161 and

357   RHJ147. The vector pGEM-T was linearized by amplification using primer RHJ144 and RHJ145. These

358   three fragments were assembled by Gibson cloning to yield pRHJ010. The fragment containing the

359   two *F. johnsoniae* chromosomal regions was then amplified from pRHJ010 with primers RHJ110 and

360   RHJ113. The resulting 5.2 kb fragment was inserted between the BamHI and KpnI sites of pYT354[29] to

361   give plasmid pRHJ011.

362   The strategy to generate point mutations in *gldL* involved the use of an intermediate cloning vector

363   that was produced as follows. A 5.3 kb region including the *gldL* gene sequence and surrounding

364   chromosomal regions was amplified using primers RHJ146 and RHJ149. pGEM-T was linearized by

365   amplification with primers RHJ144 and RHJ145. The two fragments were assembled by Gibson cloning

366   to give pRHJ012. An intermediate cloning vector for generating mutations in *gldM* was produced in an

367   analogous manner using primers RHJ147 and RHJ148 and yielding plasmid pRHJ013.

368   A suicide vector for the introduction of the *gldL(N10A)* point mutation was produced as follows.

369   pRHJ012 was linearized by amplification with primers RHJ310 and RHJ311, which introduce the

370   desired 2 bp point mutation in codon N10. The resulting fragment was re-circularised by *in vivo*

371   assembly [30], yielding plasmid pRHJ014. The fragment containing the mutated *gldL* sequence and

372   adjacent regions was then amplified from pRHJ014 with primers RHJ341 and RHJ342. The vector

373   pYT354 was linearized by digestion with BamHI and SalI. The two fragments were then assembled by

374   *in vivo* Gibson cloning to give plasmid pRHJ036. Other point mutations were generated similarly, using

375   pRHJ012 as a template for mutations in *gldL* and pRHJ013 as a template for mutations in *gldM*, using

376   the primers described in Supplementary Table 1.

377   A suicide vector to introduce a Twin-Strep tag-coding sequence to the 3′ end of *gldL* was produced

378   as follows. A 2.5-kbp fragment comprising *gldL* together with the directly upstream region was

379   amplified using primers FL265 and FL266. This fragment was inserted into the SphI and NcoI sites of

380   pGEM-T easy to generate pFL76. A 2.6-kbp fragment downstream of *gldL* was amplified using primers

381   FL267 and FL268. This fragment was inserted into the NcoI and SalI sites of pFL76 to generate pFL77.

382   A fragment encoding a TEV cleavage site followed by a Twin-Strep tag was amplified from pRHJ007

383   using primers RHJ172 and RHJ173. This fragment was inserted between the BamHI and NcoI sites of

384   pFL77 to give plasmid pRHJ058.

385   A suicide vector for the construction of a *gldL(N10A)-twinstrep* strain was produced as follows. A

386   fragment including the pGEM-T backbone, the mutation site, and a 2.3 kb region upstream of the

387   mutation site was amplified from pRHJ012 using primers RHJ311 and RHJ144. A fragment containing

388   the mutation site together with a 3.2 kb region downstream of the mutation site including the Twin-

389   Strep tag-encoding sequence was amplified from pRHJ058. These fragments were assembled by

390   Gibson cloning to give pRHJ059. The fragment containing the mutated *gldL* sequence and adjacent

391   regions was amplified using primers RHJ341 and RHJ342. pYT354 was linearised by digestion with

392   BamHI and SalI. These two fragments were assembled by Gibson cloning to give pRHJ081. Suicide

393   vectors for the construction of other *gldL* point mutations in a *gldL-twinstrep* background were

394   produced in an analogous manner using the primers described in Supplementary Table 1.

395   To introduce point mutations in *gldM* into a *gldL-twinstrep* background, the mutation site and the

396   region upstream of the *gldM* point mutation, including the Twin-Strep tag-encoding sequence of the

397   *gldL* gene, was amplified from pRHJ058. The mutation site and the region downstream of the point

398   mutation together with the pGEM-T backbone, was amplified from pRHJ013. These fragments were

399   assembled by Gibson cloning. Primers RHJ342 and RHJ343 were then used to transfer the mutated

400   *gldM* sequences into pYT354.

401   A suicide vector for the construction of *halotag-sprB* strains was produced by Gibson assembly of

402   the following four fragments yielding plasmid pAK021: pYT313 linearized with primers AK41 and AK62;

403   codons 86 to 2647 of *sprB* amplified from the *F. johnsoniae* chromosome with primers AK59 and AK60;

404   *twinstrep-halotag* amplified from plasmid pET21-ts-halo-RemA97CTD with primers AK37 and AK61; a

405   genomic fragment extending from the start of *sprD* through to codon 87 of *sprB* was amplified from

406   the *F. johnsoniae* chromosome with primers AK36 and AK40.

407   For pulse-chase experiments, a plasmid directing production of a tripartite fusion protein consisting

408   of the *F. johnsoniae* RemA signal sequence, mCherry, and the RemA C-terminal domain under the

409   control of the *remA* promoter was constructed as follows. A region encompassing 361 nucleotides

410   immediately upstream of *remA* together with the first 150 nucleotides of *remA* was amplified from

411   genomic DNA using primers PG001 and PG002, then cloned into the XbaI-SpeI restriction sites of

412   pCP11[24]. Between the SpeI and SacI sites of the resulting plasmid was inserted the coding sequence

413   for mCherry with no stop codon amplified from plasmid pRVCHYC-5[31] using primers PG003 and PG004.

414   Finally a region coding for the 97 C-terminal residues of RemA was amplified with primers PG005 and

415   PG006 and inserted between the SacI and SalI sites to produce plasmid pCP-remA$_{us}$-mch-CTD97$_{remA}$. A

416   plasmid coding for the fusion protein with a K1432A substitution in the RemA CTD was made by the

417   QuikChange mutagenesis (Agilent) using primers PG007 and PG008.

418   Suicide and expression plasmids were introduced into *F. johnsoniae* strains by biparental mating

419   using *E. coli* S17-1[32] as the donor strain, as previously described[24]. Point mutations in *gldL* were

420   introduced into the chromosome by using the Δ*gldL* strains Fl_082 or Ak_205 as the recipient. Point

421   mutations in *gldM* were introduced into the chromosome by using the Δ*gldM* strains Rhj_006 or

422   Ak_203 as the recipient. Erythromycin resistance was used to select cells with a chromosomally-

423   integrated suicide plasmid. One of the resulting clones was grown overnight in CYE without antibiotic

424   to allow for loss of the plasmid backbone, and then plated onto CYE agar containing 5 % sucrose.

425   Sucrose-resistant colonies were screened by PCR for the presence of the desired chromosomal

426   modification and then verified by sequencing.

427

Purification of PorLM and GldLM complexes

429   GldLM' proteins were overproduced from plasmids pRHJ007 and pRHJ008 as follows. Colonies of

430   BL21(DE3) cells carrying the appropriate plasmid were inoculated into 50 ml 2xYT medium and

431   cultured at 37°C with shaking for 6-8 h. The cells were diluted to $OD_{600} = 0.02$ in TB supplemented with

432   0.2 % L-rhamnose and then grown at 37°C with shaking for 14 h. Cells were harvested by centrifugation

433   at 5,000g for 15 min at 4 °C. Cells were washed once in Dulbecco A phosphate buffered saline (PBS)

434   and stored at -20°C until further use.

435   The frozen cell pellet was resuspended in 3.3 ml per g of cells of Lysis Buffer (PBS supplemented with

436   1 mM EDTA, 30 µg ml^{-1} DNase I, 400 µg ml^{-1} lysozyme, and 1 tablet per 100 ml SIGMAFAST™ protease

437   inhibitor cocktail). The cells were then disrupted using an Emulsiflex homogeniser operated at 15,000

438   PSI. The resulting lysate was centrifuged at 27,000g for 30 min at 4 °C to remove cellular debris before

439   the membrane fraction was recovered by centrifugation at 210,000g for 1 h at 4 °C. The membrane

440   pellets were stored overnight at 4 °C before being resuspended in 8 ml Resuspension Buffer (PBS, 1

441   mM EDTA) per g membrane. 1 ml 10 % (w/v) lauryl maltose neopentyl glycol (LMNG; Anatrace)

442   solution was added per g of membranes and the suspension was gently stirred at 4 °C for 2 h. Non-

443   solubilised material was removed by centrifugation at 75,000g at 10 °C for 30 min. The resulting

444   supernatant solution was passed through a 5 ml StrepTactin XT cartridge (IBA). The column was

445   washed with 10 column volumes (CV) StrepTactin Wash Buffer (PBS, 1 mM EDTA, 0.02 % LMNG)

446   .Protein was eluted in 2 CV StrepTactin Elution Buffer (PBS, 0.02 % LMNG, 1 mM EDTA, 50 mM D-

447   biotin). The elution fractions were concentrated to 500 µl using a 100 kDa MWCO Amicon Ultra–15

448   centrifugal filter, and injected on to a Superose 6 10/300 Increase GL size-exclusion chromatography

449   column (GE Healthcare) equilibrated in 20 mM HEPES pH 7.5, 150 mM NaCl, 0.02 % LMNG. Protein

450   purity was assessed by SDS-PAGE (Extended Data Figure 2a-b) and GldLM'-containing fractions were

451   pooled, concentrated using a GE Healthcare 100 kDa MWCO Vivaspin 500 concentrator, and stored at

452   4°C until use. Protein concentrations were determined spectrophotometrically using A_{280nm} 1 = 1 mg

453   ml^{-1}.

454   Production of recombinant PorLM complexes was carried out as follows. An overnight culture of *E.*

455   *coli* Mt56(DE3)[33] carrying pRHJ006 in 2xYT medium[34] was diluted 100-fold into fresh Terrific Broth

456 medium[35] containing 100 μg ml^{-1} ampicillin, and grown at 37°C with shaking to OD$_{600}$ = 4.0. Protein

457 production was then induced by addition of 0.1 mM IPTG and the cells cultured for 15 h at 24°C with

458 shaking. Cells were harvested and proteins purified as described above for the GldLM' complex, with

459 the following differences. 1 mM EDTA was omitted from the StrepTactin Elution Buffer. Following

460 elution from the StrepTactin XT cartridge, the eluted fraction was subsequently passed through a 5 ml

461 Ni-NTA Superflow cartridge (Qiagen). The column was washed with 10 CV Ni-NTA Wash Buffer 1 (PBS,

462 0.02 % LMNG, 20 mM imidazole), followed by 10 CV Ni-NTA Wash Buffer 2 (PBS, 0.02 % LMNG, 40 mM

463 imidazole). Protein was eluted in 1.2 CV Ni-NTA Elution Buffer (PBS, 0.02 % LMNG, 250 mM imidazole).

464 1mg of TEV-His$_6$ protease was added per 10 mg eluted protein and the sample dialysed overnight

465 against Dialysis Buffer (PBS, 0.02 % LMNG) in 3.5 kDa molecular weight cutoff (MWCO) SnakeSkin®

466 dialysis tubing (Thermo Scientific) at 4°C. The dialysate was centrifuged at 3,220g for 15 min at 4°C.

467 Imidazole from a 2M stock was added to the supernatant to achieve a final concentration of 20 mM.

468 The supernatant was passed over a Ni-NTA column. The flowthrough containing PorLM was collected

469 and then further processed by SEC chromatography as described for the GldLM' purification above

470 (see Extended Data Figure 1c).

471

472 **Cryo-EM sample preparation and imaging**

473   Four microlitre aliquots of purified GldLM' (A$_{280nm}$ = 0.4-0.5) or PorLM (A$_{280nm}$ = 0.2- 0.5) complexes

474 were applied onto glow-discharged holey carbon coated grids (Quantifoil 300 mesh, Au R1.2/1.3),

475 adsorbed for 10 s, blotted for 2 s at 100% humidity at 4 °C and plunge frozen in liquid ethane using a

476 Vitrobot Mark IV (FEI).

477   Data were collected in counting mode on a Titan Krios G3 (FEI) operating at 300 kV with a GIF energy

478 filter (Gatan) and K2 Summit detector (Gatan) using a pixel size of 0.822 Å and a total dose of 48 e$^-$/Å^2

479 spread over 20 fractions.

480

481 **Cryo-EM data processing**

482 Motion correction and dose weighting were performed using MotionCor implemented in Relion

483 3.0[36]. Contrast transfer functions were calculated using CTFFIND4[37]. Particles were picked in Simple[38]

484 and processed in Relion 3.0[36]. Gold standard Fourier shell correlations using the 0.143 criterion and

485 local resolution estimations were calculated within Relion[36] (Extended Data Fig. 3).

486 3,284,887 GldLM' particles were extracted from 9,858 movies in 256 x 256 pixel boxes and subjected

487 to a round of reference-free 2D classification, from which 531,515 particles were recovered. An *ab*

488 *initio* initial model was generated from a subset of 500 particles using SIMPLE[38]. This model was low-

489 pass filtered to 60 Å and used as reference for 3D classification (4 classes, 7.5° sampling) against a

490 335,887 particle subset followed by refinement which yielded a 6.8 Å map. This map was used as initial

491 reference (40 Å low-pass filtered) and mask for 3D classification (3 classes, 15 iterations at 7.5°

492 sampling then 10 iterations at 3.75° sampling) against the entire dataset and further refined to 4.0 Å.

493 Bayesian particle polishing followed by another round of 3D classification with local angular searches

494 yielded a 3.9 Å map from 119,230 particles after refinement.

495 PorLM particles (1,133,336) were extracted from 14,135 movies in 324 x 324 boxes and subjected to

496 two rounds of reference-free 2D classification, from which 495,572 particles were recovered. After

497 recentering and reextraction in a smaller box (256 x 256), particles were subjected to 3D classification

498 (4 classes, 15 iterations at 7.5° sampling then 10 iterations at 3.75° sampling) against a 40 Å low-pass

499 filtered GldLM map. Selected particles (199,929) were refined against the corresponding map (low-

500 pass filtered to 40 Å) first using a soft spherical mask of 140 Å and then with a 180 Å mask. Recentered

501 particles, now in a 324 x 324 pixel box, were refined using a spherical mask of 400 Å. Particle re-

502 centering and re-extraction in 480 x 480 pixel boxes followed by refinement using local searches with

503 a mask covering the stalk and base of PorLM yielded an 8.6 Å map.

504

GldLM model building and refinement

506   The first periplasmic domains (residues 36-224) of the *F. johnsoniae* GldM crystal structure [17] (PDB

507   6ey4) were rigid body fitted into the GldLM' cryo-EM density map using Coot [39]. All other residues

508   were built *de novo* using Coot[39] guided by TMH predictions from TMHMM[40]. Multiple rounds of

509   rebuilding in both the globally sharpened and local-resolution filtered maps and real-space refinement

510   in Phenix[41] using secondary structure, rotamer, and Ramachandran restraints yielded the final model

511   described in Table 1. Validation was performed using Molprobity[42]. Conservation analysis was carried

512   out using the Consurf server[43].

513   The GldLM' model and the C-terminal periplasmic domains (residues 225-515) of PorM (PDB 6ey5)

514   were docked into the PorLM map using Chimera [44]. Figures were prepared using UCSF ChimeraX[44] and

515   Pymol (The PyMOL Molecular Graphics System, Version 2.0 Schrödinger, LLC).

516

Antibody production

518   To produce GldL antibodies a 462-bp fragment of *gldL* spanning the cytoplasmic domain (GldL$_C$,

519   residues 66-215) was amplified from genomic DNA using primers FL125 and FL126. This fragment was

520   inserted between the NdeI and BamHI sites of pWALDO-sfGFPd. The resulting vector, pFL43, produces

521   a GldL$_C$-TEV-sfGFP-His$_8$ fusion protein.

522   To produce GldM antibodies a 1305-bp fragment of *gldM* spanning the periplasmic domain (GldM$_P$,

523   residues 78-513) was amplified from genomic DNA using primers FL128 and FL129. This fragment was

524   inserted between the NdeI and BamHI sites of pWALDO-sfGFPd. The resulting vector, pFL44, produces

525   a GldM$_P$-TEV-sfGFP-His$_8$ fusion protein.

526   *E. coli* BL21 Star (DE3) cells containing either pFL43 or pFL44 were grown in 1.2 l LB medium at 37

527   °C to OD_{600} = 0.5 mid-log phase and protein expression induced by addition of 400 µM IPTG. The cells

528   were then cultured for an additional 5 h at 20 °C. Cells were harvested by centrifugation at 6,000*g* for

529   25 min and stored at -20°C until further use. All purification steps were carried out at 4°C. Cell pellets

530   were resuspended in PBS containing 30 µg ml^{-1} DNase I, 400 µg ml^{-1} lysozyme and 1 mM

531   phenylmethylsulfonyl fluoride at a ratio of 5 ml of buffer to 1 g of cell pellet. Cells were incubated on

532   ice for 30 min before being lysed by two passages through a TS series 1.1kW cell disruptor (Constant

533   System Ltd) at 30,000 PSI. Cell debris was removed by centrifugation at 20,000*g* for 25 min. The

534   supernatant was then clarified using a 0.22 µm syringe filter unit (Millipore) and circulated through a

535   5 ml HisTrap HP column (GE Healthcare) for 2 h. The column was washed with 10 CV of PBS containing

536   10 mM imidazole and bound proteins were eluted with a 10-500 mM linear imidazole in 10 CV of PBS.

537   Peak fractions were collected, diluted with an equal volume of PBS, pH 8.0, containing 0.5 mM EDTA,

538   and dialyzed for 1 h at 4 °C against 1 l of the same buffer. TEV-His$_6$ protease was added to the pooled

539   fractions at a 1 to 100 protein mass ratio and dialysis was continued overnight at 4°C against 1 l of PBS

540   containing 0.5 mM EDTA and 1 mM DTT. The cleavage reaction was then circulated through a HisTrap

541   HP column (GE Healthcare) for 2 h and the flowthrough collected. This preparation was subjected to

542   SDS-PAGE followed by Coomassie Blue staining. The band corresponding to the recombinant protein

543   domain was excised from the gel and used by Davids Biotechnologie GmbH (Regensburg, DE) to raise

544   polyclonal antibodies.

545

546   **Preparation of samples for whole cell immunoblotting analysis of GldL and GldM**

547   Strains were grown in CYE medium for 22 h, reaching OD_{600} = 5.5-6.5. The cells in 1 ml samples of

548   the culture were harvested by centrifugation at 9,000*g* for 10 min, resuspended and washed once in

549   1 ml PBS, and finally resuspended in PBS to an OD_{600} = 5.0. These samples were then diluted ten-fold

550   in PBS, subject to SDS-PAGE, and analysed by immunoblotting with GldL$_C$ or GldM$_P$ primary antibodies,

551   and anti-Rabbit IgG HRP Conjugate (Promega) secondary antibodies.

552

553   **Measurement of chitinase secretion**

554   Cells were grown in MM for 15.5 h, reaching OD$_{600}$ = 0.75-1.25. 5 ml culture samples were subject to

555   centrifugation at 3,720g for 10 min to remove cells. Chitinase activity in the resulting supernatants

556   was determined using a fluorometric chitinase assay kit (Sigma) with the synthetic substrate 4-

557   methylumbelliferyl N,N'-diacetyl-β-D-chitobioside. Statistical analysis of the results was carried out

558   using GraphPad Prism version 7.03 for Windows (GraphPad Software, La Jolla California USA,

559   www.graphpad.com). Normality of datasets was assessed by the Kolmogorov-Smirnov test. Normally

560   distributed datasets were compared to the parental strain using one-way ANOVA followed by Dunn's

561   multiple comparison test. Non-normally distributed datasets were compared to WT using a Kruskal-

562   Wallis test followed by Dunnett's multiple comparisons test.

563

564   **Measurement of gliding motility on agar**

565   Strains were grown overnight in PY2 medium, washed once in PY2 medium, then resuspended in

566   Py2 medium to an OD$_{600}$ = 0.1. A 2 μl sample was then spotted on PY2 agar plates. Plates were

567   incubated at 25°C for 48 h before imaging with a Zeiss AXIO Zoom MRm CCD camera and Zeiss

568   software (ZenPro 2012, version 1.1.1.0).

569

570   **Microscopic observation of gliding motility on glass**

571   Strains were grown overnight in MM, diluted 40-fold into fresh medium and grown for 5 h at 25°C

572   with 50 rpm shaking. An aliquot of the culture was introduced to a tunnel slide, incubated for 5 min,

573 washed twice with 100 µl fresh medium and imaged in phase contrast on a Zeiss Axoivert 200

574 microscope fitted with a Photometrics Coolsnap HQ Camera using a 63x 1.4NA Plan-Apochromat lens.

575 Tif images were captured using Metamorph software (Molecular Devices) and then modified in Image

576 J[45]. Videos were collected at 20 frames per second with a 15 ms exposure time using 2x2 binning.

577

Single molecule fluorescence imaging of SprB mobility

579 Strains expressing the Halo Tag-SprB fusion were grown overnight in CYE medium, diluted 40-fold

580 into fresh medium and grown at 30°C with 180 rpm shaking to early stationary phase (OD_{600} = 0.8-1.0).

581 The HaloTag-SprB fusion was labelled by mixing 1 ml of this culture with 1 µl of a 10 µM stock solution

582 of PA Janelia Fluor 646 HaloTag ligand[46,47] in dimethyl sulfoxide (DMSO) and cultured for a further 30

583 min. The cells were harvested at 9000g for 3 min, washed 3 times with 650 µl PY2 medium, and then

584 2 µl cells were spotted onto a 1 % agarose pad containing 50 % PY2 medium.

585 Fluorescence images were acquired at 25°C using a Nanoimager (Oxford Nanoimaging) equipped

586 with 405nm and 640nm 1W DPSS lasers. Optical magnification was provided by a 100x oil-immersion

587 objective (Olympus, numerical aperture (NA) 1.4) and images were acquired using an ORCA-Flash4.0

588 V3 CMOS camera (Hamamatsu). Cells were imaged using a 20 ms exposure time, with the 405 nm

589 photoactivation laser at 10% power and the 640 nm measurement laser at 20% power. Different

590 strains were imaged at different strobing frequencies to accommodate the large differences in adhesin

591 velocities between the different *gldLM* mutants. Specifically, strain Ak_73 (wild type *gldLM*) was

592 imaged without strobing, strains Ak_196 (*gldL(Y13A)*), Ak_197 (*gldL(H30A)*), and Ak_199 (*gldM(Y17F)*)

593 were imaged with a 60 ms dark interval, whilst Ak_198 (*gldL(K27A)*) was imaged with a 480 ms dark

594 interval.

595 Fluorescent foci were tracked using the Nanoimager software. Helical tracks were exported as csv

596 files and the average frame to frame displacement calculated. The resulting data were analysed using

597   GraphPad Prism version 7.03 for Windows (GraphPad Software, La Jolla California USA,

598   www.graphpad.com), using a Kruskal-Wallis test followed by Dunn's multiple comparisons test. The

599   data were plotted using Prism.

600

601   Pulse-chase assay of Type 9 protein export

602   The required *F. johnsoniae* strain was inoculated from a freshly-streaked plate into 5 ml SDY medium

603   (SD medium[48] containing 0.01% yeast extract) and cultured for 24 h at 30 °C with shaking. The cultures

604   were harvested by centrifugation, resuspended in the same volume of SDAC (SD medium with 0.04

605   mg ml^{-1} of all L-amino acids except methionine plus 1.5% CYE medium), then diluted one in five in

606   fresh SDAC. These cultures were grown for 2.5 h at 30 °C and 30 rpm shaking. 40 µCi ml^{-1} EasyTag L-

607   [^{35}S]-methionine (Perkin-Elmer) was then added and growth was continued for 30 min. Cultures were

608   harvested by centrifugation and resuspended in the same volume of unlabelled SDAC containing 0.4

609   mg ml^{-1} unlabelled L-methionine, and where required, either 10 µM carbonyl cyanide *m*-chlorophenyl

610   hydrazone (CCCP) or 10 mM sodium arsenate. The cultures were further incubated with shaking at 30

611   °C. At appropriate time points 1 ml samples were removed from each culture and the cells pelleted by

612   centrifugation. Cells were resuspended in RIPA buffer (10 mM Tris-HCl pH 7.5, 150 mM NaCl, 0.5 mM

613   EDTA, 0.1% SDS, 1% Triton X-100, 1% deoxycholate, 0.09% sodium azide). Both the resuspended

614   pellets and culture supernatants stored at 4 °C until the end of the time course, at which point all

615   samples were incubated for a further 1 hour at 4 °C. The cell pellet samples were then diluted with

616   1.5 volumes of RND buffer (10 mM Tris-HCl pH 7.5, 150 mM NaCl, 0.5 mM EDTA), centrifuged for 10

617   min at 13,000*g* and the supernatant retained. Both these cell pellet-derived samples and the culture

618   supernatant samples were incubated with 10 µl RFP-trap MA (Chromotek) for one hour at 24 °C with

619   constant mixing. The RFP-trap resin was isolated on a magnetic rack and washed with 2 x 800 µl RND

620   buffer, then resuspended in SDS-PAGE sample buffer. Samples were separated by SDS-PAGE, and the

621   resulting gels fixed, dried and exposed to radiographic film (GE Healthcare).

622

Measurement of cellular ATP levels

624   Strains were cultured as for the pulse-chase experiments to the point at which the cells were

625   transferred to SDAC medium. The cells were then incubated for 3 h at 30 ˚C and 110 rpm. 0.5 ml

626   samples were treated with 10 µM CCCP, or 10 mM sodium arsenate, or left untreated for 20 min at

627   24 ˚C. Cellular ATP levels were then determined using an ATP Bioluminescence Assay Kit HS II (Roche).

628   Cells were diluted to OD_{600} = 0.1 with dilution buffer from the kit. 200 µl aliquots of diluted cells were

629   combined with 200 µl lysis buffer from the kit and incubated at 70 ˚C for 5 min. Lysates were

630   immediately transferred to ice and then clarified by centrifugation. The ATP content in the lysates was

631   determined according to the kit manufacturer's instructions and using a CLARIOstar Plus plate reader

632   (BMG Labtech). Statistical analysis of cellular ATP levels was carried out using R [49].

633

References

635   1   Nicholls, D. G. & Ferguson, S. J. Bioenergetics 4. *Bioenergetics 4*, 1-419 (2013).
636   2   Guo, H. & Rubinstein, J. L. Cryo-EM of ATP synthases. *Curr Opin Struct Biol* **52**, 71-79,
637   doi:10.1016/j.sbi.2018.08.005 (2018).
638   3   Walker, J. E. The ATP synthase: the understood, the uncertain and the unknown. *Biochem Soc*
639   *Trans* **41**, 1-16, doi:10.1042/BST20110773 (2013).
640   4   Sowa, Y. & Berry, R. M. Bacterial flagellar motor. *Q Rev Biophys* **41**, 103-132,
641   doi:10.1017/S0033583508004691 (2008).
642   5   Kojima, S. Dynamism and regulation of the stator, the energy conversion complex of the
643   bacterial flagellar motor. *Curr Opin Microbiol* **28**, 66-71, doi:10.1016/j.mib.2015.07.015
644   (2015).
645   6   Celia, H. *et al.* Cryo-EM structure of the bacterial Ton motor subcomplex ExbB-ExbD provides
646   information on structure and stoichiometry. *Commun Biol* **2**, 358, doi:10.1038/s42003-019-
647   0604-2 (2019).
648   7   Cascales, E., Lloubes, R. & Sturgis, J. N. The TolQ-TolR proteins energize TolA and share
649   homologies with the flagellar motor proteins MotA-MotB. *Mol Microbiol* **42**, 795-807,
650   doi:10.1046/j.1365-2958.2001.02673.x (2001).
651   8   McBride, M. J. Bacteroidetes Gliding Motility and the Type IX Secretion System. *Microbiol*
652   *Spectr* **7**, doi:10.1128/microbiolspec.PSIB-0002-2018 (2019).
653   9   Nakane, D., Sato, K., Wada, H., McBride, M. J. & Nakayama, K. Helical flow of surface protein
654   required for bacterial gliding motility. *Proc Natl Acad Sci U S A* **110**, 11145-11150,
655   doi:10.1073/pnas.1219753110 (2013).

10   Ridgway, H. F. Source of energy for gliding motility in Flexibacter polymorphus: effects of metabolic and respiratory inhibitors on gliding movement. *J Bacteriol* **131**, 544-556 (1977).

11   Shrivastava, A., Lele, P. P. & Berg, H. C. A rotary motor drives Flavobacterium gliding. *Curr Biol* **25**, 338-341, doi:10.1016/j.cub.2014.11.045 (2015).

12   Shrivastava, A., Roland, T. & Berg, H. C. The Screw-Like Movement of a Gliding Bacterium Is Powered by Spiral Motion of Cell-Surface Adhesins. *Biophys J* **111**, 1008-1013, doi:10.1016/j.bpj.2016.07.043 (2016).

13   Nelson, S. S., Bollampalli, S. & McBride, M. J. SprB is a cell surface component of the Flavobacterium johnsoniae gliding motility machinery. *J Bacteriol* **190**, 2851-2857, doi:10.1128/JB.01904-07 (2008).

14   Shrivastava, A. & Berg, H. C. A molecular rack and pinion actuates a cell-surface adhesin and enables bacterial gliding motility. *Science Advances* **6**, 1-6, doi:10.1126/sciadv.aay6616 (2020).

15   Shrivastava, A., Johnston, J. J., van Baaren, J. M. & McBride, M. J. Flavobacterium johnsoniae GldK, GldL, GldM, and SprA are required for secretion of the cell surface gliding motility adhesins SprB and RemA. *J Bacteriol* **195**, 3201-3212, doi:10.1128/JB.00333-13 (2013).

16   Vincent, M. S. *et al.* Characterization of the Porphyromonas gingivalis Type IX Secretion Trans-envelope PorKLMNP Core Complex. *J Biol Chem* **292**, 3252-3261, doi:10.1074/jbc.M116.765081 (2017).

17   Leone, P. *et al.* Type IX secretion system PorM and gliding machinery GldM form arches spanning the periplasmic space. *Nat Commun* **9**, 429, doi:10.1038/s41467-017-02784-7 (2018).

18   Gorasia, D. G. *et al.* Structural Insights into the PorK and PorN Components of the Porphyromonas gingivalis Type IX Secretion System. *PLoS Pathog* **12**, e1005820, doi:10.1371/journal.ppat.1005820 (2016).

19   Sato, K. *et al.* A protein secretion system linked to bacteroidete gliding motility and pathogenesis. *Proc Natl Acad Sci U S A* **107**, 276-281, doi:10.1073/pnas.0912010107 (2010).

20   Lauber, F., Deme, J. C., Lea, S. M. & Berks, B. C. Type 9 secretion system structures reveal a new protein transport mechanism. *Nature* **564**, 77-82, doi:10.1038/s41586-018-0693-y (2018).

21   Veith, P. D., Glew, M. D., Gorasia, D. G. & Reynolds, E. C. Type IX secretion: the generation of bacterial cell surface coatings involved in virulence, gliding motility and the degradation of complex biopolymers. *Mol Microbiol* **106**, 35-53, doi:10.1111/mmi.13752 (2017).

22   Lasica, A. M., Ksiazek, M., Madej, M. & Potempa, J. The Type IX Secretion System (T9SS): Highlights and Recent Insights into Its Structure and Function. *Front Cell Infect Microbiol* **7**, 215, doi:10.3389/fcimb.2017.00215 (2017).

23   von Heijne, G. & Gavel, Y. Topogenic signals in integral membrane proteins. *Eur J Biochem* **174**, 671-678, doi:10.1111/j.1432-1033.1988.tb14150.x (1988).

24   McBride, M. J. & Kempf, M. J. Development of techniques for the genetic manipulation of the gliding bacterium Cytophaga johnsonae. *J Bacteriol* **178**, 583-590 (1996).

25   Liu, J., McBride, M. J. & Subramaniam, S. Cell surface filaments of the gliding bacterium Flavobacterium johnsoniae revealed by cryo-electron tomography. *J Bacteriol* **189**, 7503-7506, doi:10.1128/JB.00957-07 (2007).

26   Agarwal, S., Hunnicutt, D. W. & McBride, M. J. Cloning and characterization of the Flavobacterium johnsoniae (Cytophaga johnsonae) gliding motility gene, gldA. *Proc Natl Acad Sci U S A* **94**, 12139-12144 (1997).

27   Dietsche, T. *et al.* Structural and Functional Characterization of the Bacterial Type III Secretion Export Apparatus. *PLoS Pathog* **12**, e1006071, doi:10.1371/journal.ppat.1006071 (2016).

28   Drew, D., Lerch, M., Kunji, E., Slotboom, D. J. & de Gier, J. W. Optimization of membrane protein overexpression and purification using GFP fusions. *Nat Methods* **3**, 303-313, doi:10.1038/nmeth0406-303 (2006).

706   29   Zhu, Y. *et al.* Genetic analyses unravel the crucial role of a horizontally acquired alginate lyase
707   for brown algal biomass degradation by Zobellia galactanivorans. *Environ Microbiol* **19**, 2164-
708   2181, doi:10.1111/1462-2920.13699 (2017).
709   30   Jacobus, A. P. & Gross, J. Optimal cloning of PCR fragments by homologous recombination in
710   Escherichia coli. *PloS one* **10**, e0119221, doi:10.1371/journal.pone.0119221 (2015).
711   31   Thanbichler, M., Iniesta, A. A. & Shapiro, L. A comprehensive set of plasmids for vanillate- and
712   xylose-inducible gene expression in Caulobacter crescentus. *Nucleic Acids Res* **35**, e137,
713   doi:10.1093/nar/gkm818 (2007).
714   32   Simon, R., Priefer, U. & Puhler, A. A Broad Host Range Mobilization System for Invivo Genetic-
715   Engineering - Transposon Mutagenesis in Gram-Negative Bacteria. *Bio-Technology* **1**, 784-791,
716   doi:DOI 10.1038/nbt1183-784 (1983).
717   33   Baumgarten, T. *et al.* Isolation and characterization of the E. coli membrane protein
718   production strain Mutant56(DE3). *Sci Rep* **7**, 45089, doi:10.1038/srep45089 (2017).
719   34   Miller, J. *Experiments in Molecular Genetics*. (Cold Spring Harbor, 1972).
720   35   Tartof, K. D. a. H., C.A. . Improved media for growing plasmid and cosmid clones. *Focus®* **9**, 12
721   (1987).
722   36   Zivanov, J., Nakane, T. & Scheres, S. H. W. A Bayesian approach to beam-induced motion
723   correction in cryo-EM single-particle analysis. *IUCrJ* **6**, 5-17, doi:10.1107/S205225251801463X
724   (2019).
725   37   Rohou, A. & Grigorieff, N. CTFFIND4: Fast and accurate defocus estimation from electron
726   micrographs. *J Struct Biol* **192**, 216-221, doi:10.1016/j.jsb.2015.08.008 (2015).
727   38   Reboul, C. F., Eager, M., Elmlund, D. & Elmlund, H. Single-particle cryo-EM-Improved ab initio
728   3D reconstruction with SIMPLE/PRIME. *Protein Sci* **27**, 51-61, doi:10.1002/pro.3266 (2018).
729   39   Emsley, P., Lohkamp, B., Scott, W. G. & Cowtan, K. Features and development of Coot. *Acta
730   Crystallogr D Biol Crystallogr* **66**, 486-501, doi:10.1107/S0907444910007493 (2010).
731   40   Krogh, A., Larsson, B., von Heijne, G. & Sonnhammer, E. L. Predicting transmembrane protein
732   topology with a hidden Markov model: application to complete genomes. *J Mol Biol* **305**, 567-
733   580, doi:10.1006/jmbi.2000.4315 (2001).
734   41   Afonine, P. V. *et al.* Real-space refinement in PHENIX for cryo-EM and crystallography. *Acta
735   Crystallogr D Struct Biol* **74**, 531-544, doi:10.1107/S2059798318006551 (2018).
736   42   Williams, C. J. *et al.* MolProbity: More and better reference data for improved all-atom
737   structure validation. *Protein Sci* **27**, 293-315, doi:10.1002/pro.3330 (2018).
738   43   Ashkenazy, H. *et al.* ConSurf 2016: an improved methodology to estimate and visualize
739   evolutionary conservation in macromolecules. *Nucleic Acids Res* **44**, W344-350,
740   doi:10.1093/nar/gkw408 (2016).
741   44   Goddard, T. D. *et al.* UCSF ChimeraX: Meeting modern challenges in visualization and analysis.
742   *Protein Sci* **27**, 14-25, doi:10.1002/pro.3235 (2018).
743   45   Schneider, C. A., Rasband, W. S. & Eliceiri, K. W. NIH Image to ImageJ: 25 years of image
744   analysis. *Nature methods* **9**, 671-675, doi:10.1038/nmeth.2089 (2012).
745   46   Grimm, J. B., Brown, T. A., English, B. P., Lionnet, T. & Lavis, L. D. Synthesis of Janelia Fluor
746   HaloTag and SNAP-Tag Ligands and Their Use in Cellular Imaging Experiments. *Methods Mol
747   Biol* **1663**, 179-188, doi:10.1007/978-1-4939-7265-4_15 (2017).
748   47   Grimm, J. B. *et al.* Bright photoactivatable fluorophores for single-molecule imaging. *Nature
749   methods* **13**, 985-988, doi:10.1038/nmeth.4034 (2016).
750   48   Chang, L. Y. E. & Pate, J. L. Nutritional-Requirements of Cytophaga-Johnsonae and Some of Its
751   Auxotrophic Mutants. *Curr Microbiol* **5**, 235-240 (1981).
752   49   R: A language and environment for statistical computing (R Foundation for Statistical
753   Computing, Vienna, Austria, 2017).
754   50   Kulkarni, S. S., Zhu, Y., Brendel, C. J. & McBride, M. J. Diverse C-Terminal Sequences Involved
755   in Flavobacterium johnsoniae Protein Secretion. *J Bacteriol* **199**, doi:10.1128/JB.00884-16
756   (2017).

757   51   Nijeholt, J. A. L. A. & Driessen, A. J. M. The bacterial Sec-translocase: structure and mechanism.
758   *Philos T R Soc B* **367**, 1016-1028, doi:10.1098/rstb.2011.0201 (2012).
759   52   Kamisetty, H., Ovchinnikov, S. & Baker, D. Assessing the utility of coevolution-based residue-
760   residue contact predictions in a sequence- and structure-rich era. *Proc Natl Acad Sci U S A* **110**,
761   15674-15679, doi:10.1073/pnas.1314045110 (2013).
762   53   Krissinel, E. & Henrick, K. Inference of macromolecular assemblies from crystalline state.
763   *Journal of Molecular Biology* **372**, 774-797 (2007).
764   54   McBride, M. J. & Braun, T. F. GldI is a lipoprotein that is required for Flavobacterium
765   johnsoniae gliding motility and chitin utilization. *J Bacteriol* **186**, 2295-2302 (2004).

766

767

768   **Data availability**

769   The cryo-EM volumes have been deposited in the Electron Microscopy Data Bank (EMDB) with

770   accession codes EMD-10893 and EMD-10894, and the coordinates have been deposited in the

771   Protein Data Bank (PDB) with accession code 6YS8. Source Data are available with the online version

772   of the paper.

773   **Extended data figures and tables**

774
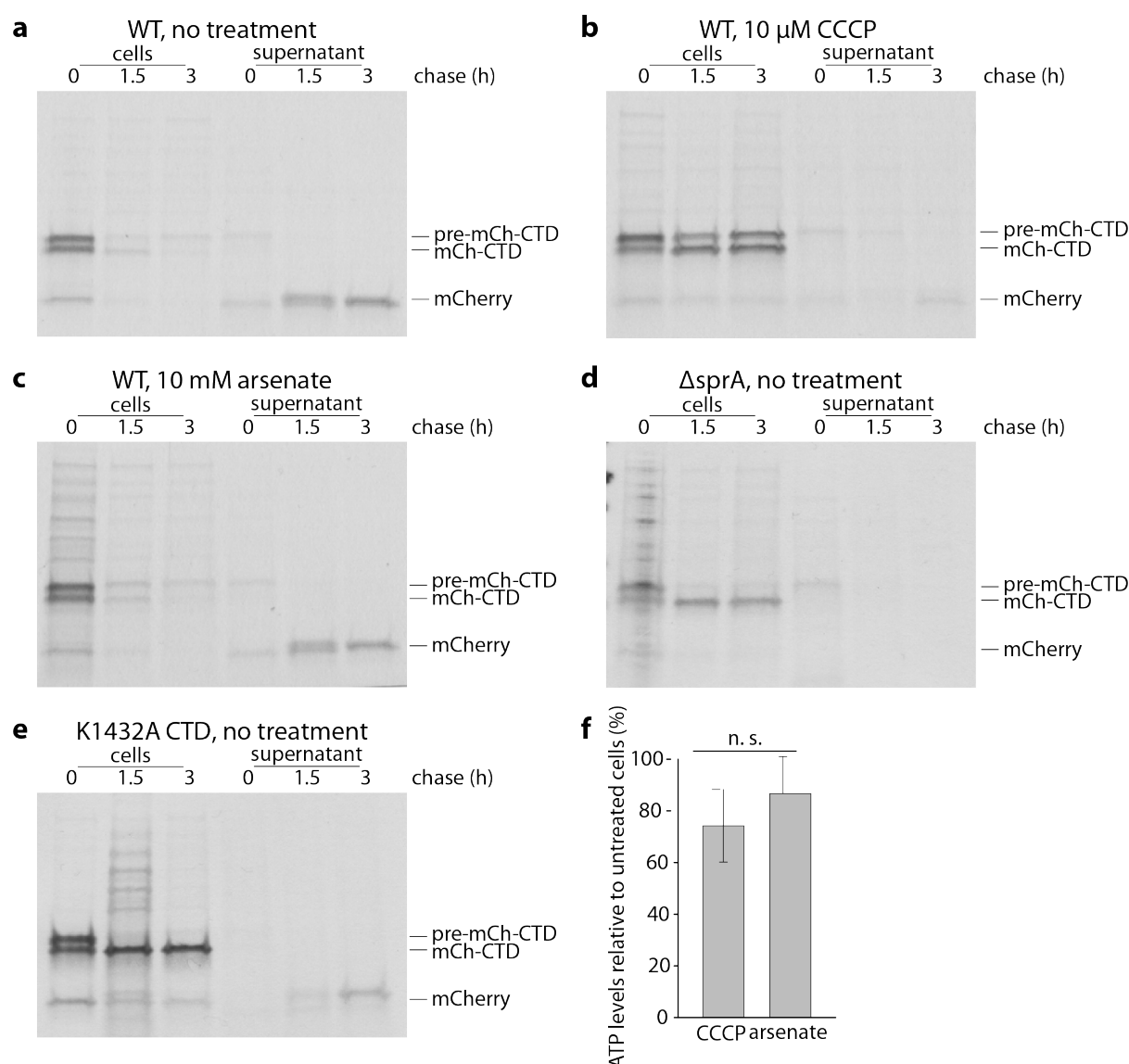
**Extended Data Fig. 1 | Protein export by the T9SS requires the protonmotive force**

a-e, Pulse-chase analysis of the export of a signal sequence-mCherry-CTD (T9SS-targeting C-terminal domain) fusion protein by the *F. johnsoniae* T9SS. Cells were labelled with [35S]methionine for 30 min, chased with cold methionine for 0 to 3 h (as indicated), and then separated into cell and supernatant (culture medium) fractions. Fusion protein was enriched by anti-mCherry immunoprecipitation and then analysed by SDS-PAGE and autoradiography. Similar data were obtained for two biological repeats. Pre-mCh-CTD, full length fusion protein; mCh-CTD, fusion protein from which the signal sequence has been removed; mCh, mCherry from which both the signal sequence and CTD have been removed. Export of the fusion protein was blocked by treatment with the protonophore carbonyl cyanide m-chlorophenyl hydrazone (CCCP, panel **b**) but not by the ATP synthase inhibitor arsenate (panel, **c**). Control experiments confirm that the observed export of the mCherry fusion requires the T9SS (Δ*sprA* strain Fl_004 [20], panel **d**) and a functional CTD (non-functional K1432A CTD[50], panel **e**). Note, that transport of the fusion across the cytoplasmic membrane by the Sec apparatus is also

789   inhibited by CCCP (panel **c**) in agreement with previous observations in *Escherichia coli*[51]. **f,**
790   Measurements of whole cell ATP levels confirm that the effects of CCCP on protein transport are not
791   an indirect effect of decreased cellular ATP. Bioluminescence readings from treated cells were
792   normalised to those of untreated cells from the same starting culture. CCCP and arsenate
793   concentrations were as in panels **b**) and **c**). Error bars represent 1 SD (10 biological repeats). The
794   datasets were tested for normality using the Shapiro-Wilk test and also inspected visually using Q-Q
795   plots. The Bartlett test was used to establish that the variances of the two datasets were likely
796   homogeneous. An independent two-tailed t-test indicated that the ATP levels in CCCP- and arsenate-
797   treated cells were not significantly different (n.s.) (t-value = -1.9619, df = 17.994, p-value =
798   0.06543>0.05) even though only CCCP treatment blocks T9SS protein export.
799

800

801
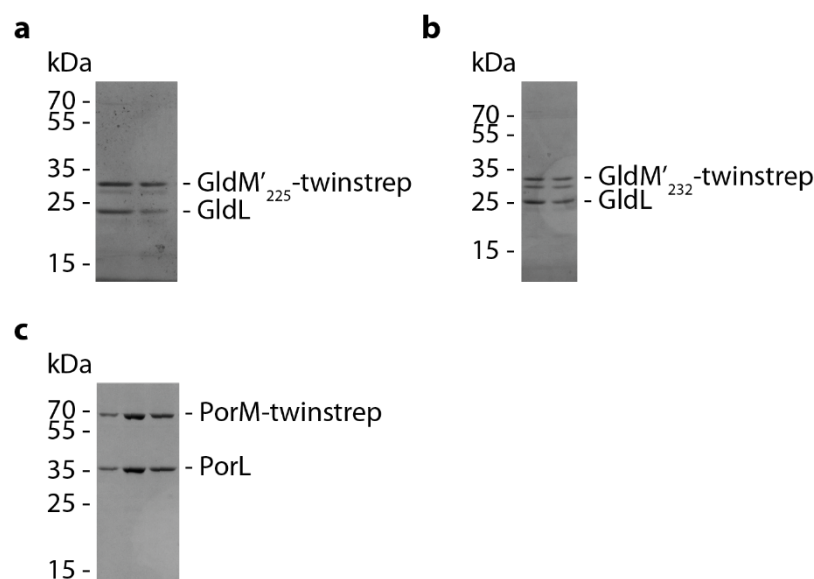
**Extended Data Fig. 2|Purification of the GldLM and PorLM complexes.**

803

Coomassie Blue-stained SDS-PAGE gels of the (**a**) GldLM$_{225}$(produced from pRHJ007), (**b**) GldLM$_{232}$ (produced from pRHJ008), and (**c**) PorLM (produced from pRHJ006) complexes used for cryo-EM structure determination. In each case the size exclusion column fractions that were pooled to make the cryo-EM grids are shown.

808

809

810
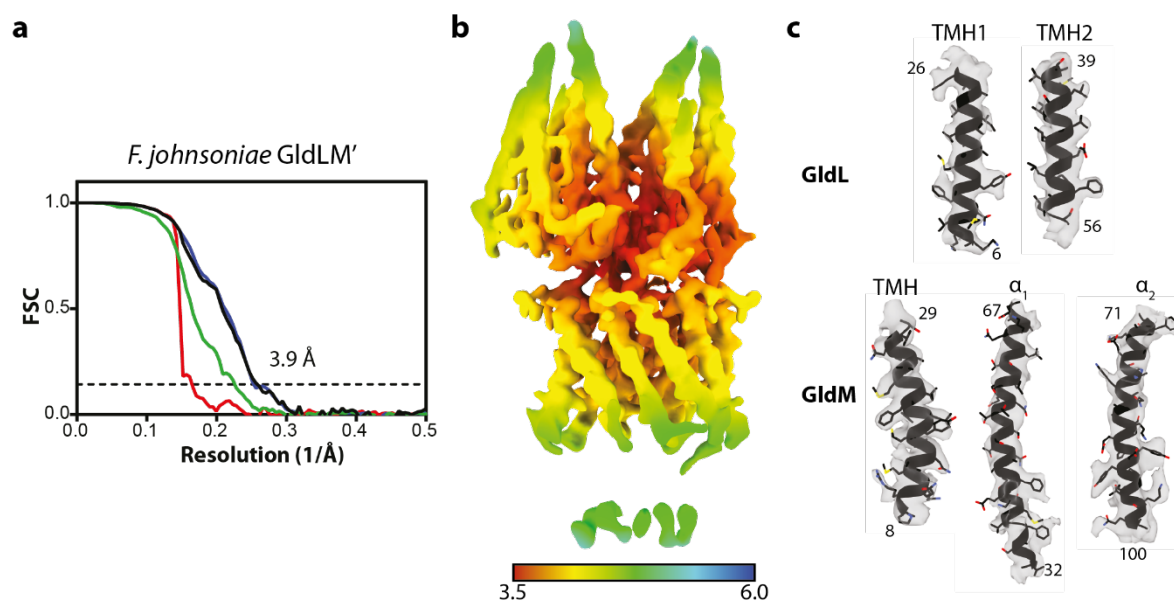
Extended Data Fig. 3 | Cryo-EM map quality and resolution estimates.

a Fourier Shell Correlation (FSC) plot for the GldLM' structure. The resolution at the gold-standard cutoff (FSC = 0.143) is indicated by the dashed line. Curves: Red, phase-randomized; Green, unmasked; blue, masked; black, MTF-corrected **b** Local resolution estimates (in Å) for the sharpened GldLM' map. **c** Representative modelled densities.

816

817

818
819
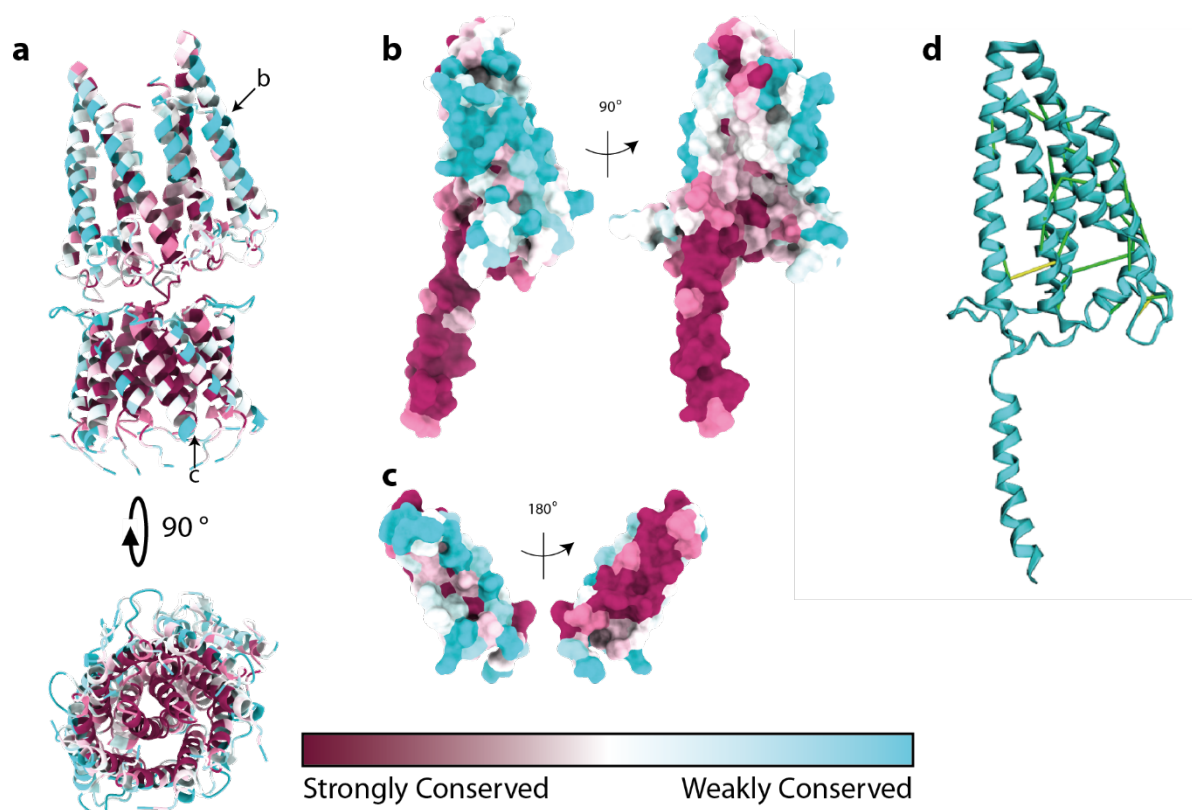
Extended Data Fig. 4 | Conservation analysis of the GldLM complex.

821

a-c, Sequence conservation assessed using Consurf[43]. **a,** The whole complex in cartoon representation. The chains shown individually in **b** and **c** are indicated with black arrows. **b,** GldM (chain B) and **c,** GldL (chain F) in surface representation. The left hand panels show the chains in the same orientation as the upper panel of **a**. **d,** Covarying residue pairs in the first periplasmic domain of GldM identified using the Gremlin server [52]. The highest-scoring pairs (score cut-off 1.63) are shown on the structure of the GldLM' complex presented here. Contacts with a minimum atom-atom distance of <5 Å are shown in green, and 5-10 Å in yellow. Note, that no high-scoring intermolecular pairs were observed.

829

830
831
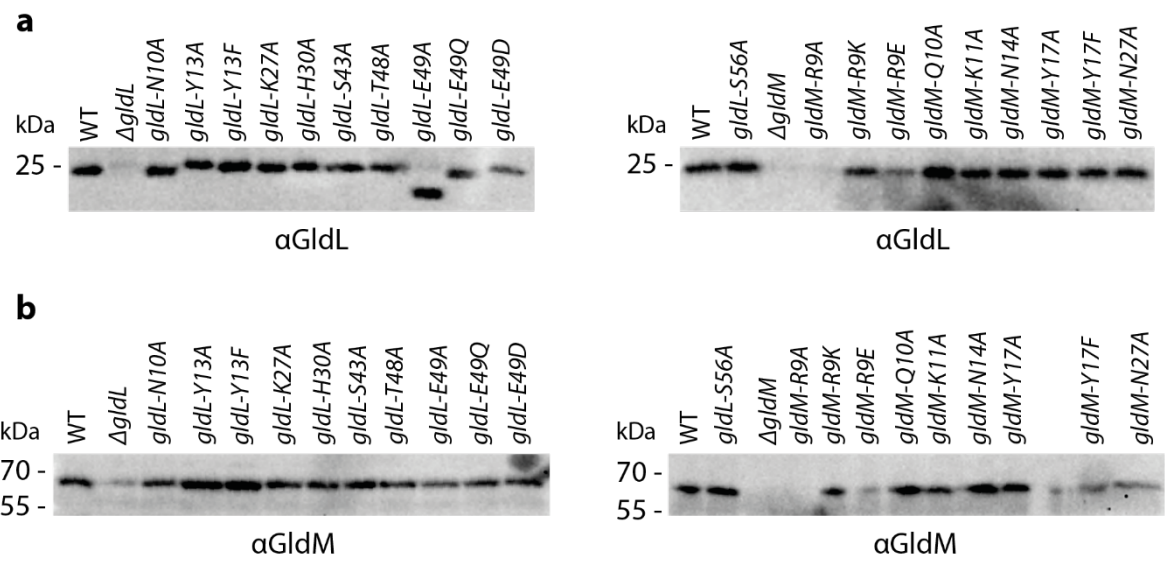
Extended Data Fig. 5 | GldL and GldM expression levels in *gldL* and *gldM* mutant strains.

Whole cell immunoblotting of the indicated strains for the presence of (**a**) GldL and (**b**) GldM. Similar data were obtained for three independent preparations.

841 **Extended Data Table 1:** Cryo-EM data collection, refinement and validation statistics.

	F. johnsoniae GldLM (EMD-10893) (PDB 6YS8)	P. gingivalis PorLM (EMD-10894)
Data collection and processing		
Magnification	165,000	165,000
Voltage (kV)	300	300
Electron exposure (e–/Å2)	48	48
Defocus range (μm)	1.0-3.0	1.0-3.0
Pixel size (Å)	0.822	0.822
Symmetry imposed	C1	C1
Initial particle images (no.)	3,284,887	1,133,336
Final particle images (no.)	119,230	199,929
Map resolution (Å)	3.9	8.6
FSC threshold	0.143	0.143
Map resolution range (Å)	3.5-5.8	
Refinement		
Initial model used (PDB code)	None	
Model resolution (Å)	3.9	
FSC threshold	0.143	
Model resolution range (Å)	3.5-5.8	
Map sharpening B factor (Å2)	-131	
Model composition		
Non-hydrogen atoms	5624	
Protein residues	737	
Ligands	0	
B factors (Å2)		
Protein	117	
Ligand	NA	
R.m.s. deviations		
Bond lengths (Å)	0.007	
Bond angles (°)	1.186	
Validation		
MolProbity score	2.22	
Clashscore	10.52	
Poor rotamers (%)	1.70	
Ramachandran plot		
Favored (%)	91.42	
Allowed (%)	6.36	
Disallowed (%)	2.21	

842

843 **Extended Data Table 2 | Contacts between the periplasmic loops of GldL and GldM.**

844 The PDBePISA server (http://www.ebi.ac.uk/pdbe/pisart.html)[53]was used to calculate the sizes of
845 the interfaces between the periplasmic loops of each copy of GldL and the periplasmic
846 domains of GldM. The periplasmic loops of GldL were taken to include residues 29-41.

GldM Copy	GldL Copy	GldL Buried Surface area (Å^2)	Number of GldL Residues	GldL Residues	GldM Residues
A	C	265.4	8	Thr29, His30, Phe31, Glu32, Thr37, Gly38, Thr39, Val40	Arg120, Asp122, Asp125, Asp126, Phe 128, Thr129, Gly130, Lys193
A	D	107.4	3	Thr29, His30, Thr39	Met26, Lys30, Glu116, Ala117, Asp119, Arg120
A	E	139.5	4	Thr29, His30, Phe31, Glu32	Met26, Asn27, Ser29, Lys30, Glu31
A	F	125.8	3	His30, Thr37, Thr39	Lys180, Glu181, Ile183
A	G	183.8	4	Thr29, His30, Thr37, Thr39	Thr129, Gly130, Asp131, Asn179, Ile183, Lys184, Glu185
B	C	-	-	-	-
B	D	-	-	-	-
B	E	64.4	5	Phe31, Glu32, Thr37, Thr39, Val40	Arg120, Asp122, Lys180, Gly194
B	F	97.2	2	Thr29, His30	Val28, Ser29, Ile33, Glu116, Ala117, Asp119
B	G	18.1	1	His30	Met26

847

848

849 **Extended Data Table 3 |** Gliding motility and T9SS phenotypes of mutant strains.

Strain	Gliding on PY2 agar	Gliding on glass	Chitinase assay (arbitrary units ± s.d.)	SprB propulsion (nm s^{-1} ± s.d.)	GldL stability	GldM stability
WT	+++	Glides normally	1.00 ± 0.2	1358 ± 900	Present	Present
Δ$gldL$	-	Does not adhere	0.00 ± 0.0	n.d.	None	Reduced
$gldL_{N10A}$	+++	Glides normally	1.09 ± 0.3	n.d.	Present	Present
$gldL_{y13A}$	-	Adheres, does not glide	0.41 ± 0.1	275 ± 100	Present	Present
$gldL_{Y13F}$	-	Adheres, does not glide	1.37 ± 0.5	n.d.	Present	Present
$gldL_{K27A}$	-	Adheres, does not glide	0.40 ± 0.1	31 ± 20	Present	Present
$gldL_{H30A}$	++	Glides slowly	1.16 ± 0.2	524 ± 200	Present	Present
$gldL_{S43A}$	+++	Glides normally	0.96 ± 0.3	n.d.	Present	Present
$gldL_{T48A}$	+++	Glides normally	1.15 ± 0.6	n.d.	Present	Present
$gldL_{E49A}$	-	Does not adhere	0.00 ± 0.0	n.d.	Clipped	Present
$gldL_{E49Q}$	-	Does not adhere	0.00 ± 0.0	n.d.	Present	Present
$gldL_{E49D}$	-	Very few cells adhere	0.02 ± 0.0	n.d.	Present	Present
$gldL_{S56A}$	+++	Glides normally	0.88 ± 0.2	n.d.	Present	Present
Δ$gldM$	-	Does not adhere	0.00 ± 0.0	n.d.	None	None
$gldM_{R9A}$	-	Does not adhere	0.00 ± 0.0	n.d.	None	None
$gldM_{R9K}$	++	Glides slowly	0.95 ± 0.2	486 ± 200	Present	Present
$gldM_{R9E}$	-	Does not adhere	0.01 ± 0.0	n.d.	Reduced	Reduced

$gldM_{Q10A}$	+++	Glides normally	0.98 ± 0.3	n.d.	Present	Present
$gldM_{K11A}$	+++	Glides normally	0.91 ± 0.1	n.d.	Present	Present
$gldM_{N14A}$	+++	Glides normally	1.10 ± 0.3	n.d.	Present	Present
$gldM_{Y17A}$	-	Adheres, does not glide	0.11 ± 0.0	n.d.	Present	Present
$gldM_{Y17F}$	+	Glides slowly	1.13 ± 0.4	774 ± 400	Present	Present
$gldM_{N27A}$	+++	Glides normally	1.30 ± 0.5	n.d.	Present	Present

850

851

852

853 **Extended Data Table 4 |** Bacterial strains used in this study.

Strain	Genotype	Reference
E. coli		
S17-1	*pro, res⁻ hsdR17 (rK⁻ mK⁺) recA⁻, RP4-2-Tc::Mu-Km::Tn7*, Tpr	32
BL21 Star™ (DE3)	F⁻ *ompT hsdS$_B$ (r$_B$-, m$_B$-) gal dcm rne*131 (DE3)	Invitrogen
F. johnsoniae		
UW101		54
Fl_004	UW101 Δ*sprA*	20
Fl_030	UW101 Δ*porV*	20
Fl_082	UW101 Δ*gldL*	This study
Rhj_006	UW101 Δ*gldM*	This study
Rhj_004	UW101 *gldL-twinstrep*	This study
Rhj_017	UW101 *gldL$_{N10A}$*	This study
Rhj_018	UW101 *gldL$_{Y13A}$*	This study
Rhj_024	UW101 *gldL$_{Y13F}$*	This study
Rhj_019	UW101 *gldL$_{K27A}$*	This study
Rhj_011	UW101 *gldL$_{H30A}$*	This study
Rhj_013	UW101 *gldL$_{S43A}$*	This study
Rhj_020	UW101 *gldL$_{T48A}$*	This study
Rhj_021	UW101 *gldL$_{E49A}$*	This study
Rhj_022	UW101 *gldL$_{E49Q}$*	This study
Rhj_025	UW101 *gldL$_{E49D}$*	This study
Rhj_023	UW101 *gldL$_{S56A}$*	This study
Rhj_035	UW101 *gldM$_{R9A}$*	This study
Rhj_032	UW101 *gldM$_{R9K}$*	This study
Rhj_029	UW101 *gldM$_{R9E}$*	This study
Rhj_012	UW101 *gldM$_{Q10A}$*	This study
Rhj_030	UW101 *gldM$_{K11A}$*	This study
Rhj_016	UW101 *gldM$_{N14A}$*	This study
Rhj_014	UW101 *gldM$_{Y17A}$*	This study
Rhj_015	UW101 *gldM$_{Y17F}$*	This study
Rhj_028	UW101 *gldM$_{N27A}$*	This study
Rhj_031	UW101 *gldL$_{N10A}$-twinstrep*	This study
Rhj_033	UW101 *gldL$_{Y13A}$-twinstrep*	This study
Rhj_041	UW101 *gldL$_{Y13F}$-twinstrep*	This study
Rhj_053	UW101 *gldL$_{K27A}$-twinstrep*	This study
Rhj_027	UW101 *gldL$_{H30A}$-twinstrep*	This study
Rhj_042	UW101 *gldL$_{S43A}$-twinstrep*	This study
Rhj_034	UW101 *gldL$_{T48A}$-twinstrep*	This study
Rhj_039	UW101 *gldL$_{E49A}$-twinstrep*	This study
Rhj_026	UW101 *gldL$_{E49Q}$-twinstrep*	This study
Rhj_050	UW101 *gldL$_{E49D}$-twinstrep*	This study
Rhj_038	UW101 *gldL$_{S56A}$-twinstrep*	This study
Rhj_049	UW101 *gldL-twinstrep gldM$_{R9A}$*	This study
Rhj_045	UW101 *gldL-twinstrep gldM$_{R9K}$*	This study
Rhj_040	UW101 *gldL-twinstrep gldM$_{R9E}$*	This study
Rhj_046	UW101 *gldL-twinstrep gldM$_{Q10A}$*	This study
Rhj_044	UW101 *gldL-twinstrep gldM$_{K11A}$*	This study
Rhj_051	UW101 *gldL-twinstrep gldM$_{N14A}$*	This study
Rhj_43	UW101 *gldL-twinstrep gldM$_{Y17A}$*	This study
Rhj_37	UW101 *gldL-twinstrep gldM$_{Y17F}$*	This study
Rhj_052	UW101 *gldL-twinstrep gldM$_{N27A}$*	This study
Ak_73	UW101 Δ*porV halotag::sprB*	This study
Ak_203	AK_73 Δ*gldM*	This study
Ak_205	AK_73 Δ*gldL*	This study
Ak_196	AK_73 *gldL$_{Y13A}$*	This study
Ak_197	AK_73 *gldL$_{H30A}$*	This study
Ak_198	AK_73 *gldL$_{K27A}$*	This study
Ak_199	AK_73 *gldM$_{Y17F}$*	This study
Ak_289	Ak_73 *gldM$_{R9K}$*	This study

854

855 **Extended Data Table 5 |** Plasmids used in this study.

Plasmid	Description[a]	Reference
pGEM-T	General cloning vector; Ap^r	Promega
pWALDO-sfGFPd	pET28(a+) derived expression vector fusing a TEV cleavage site, superfolder GFP, and a His$_8$ tag to the C-terminus of the expressed protein; Kan^r	[28]
pCDFDuet-1	Co-expression of two *orfs* under the control of T7*lac* promoters; *ori* CDF, Sm^r	Novagen
pETDuet-1	Co-expression of two *orfs* under the control of T7*lac* promoters; *ori* ColE1, Ap^r	Novagen
pT12_SpaPQR^{3xFLAG}	Encodes *Salmonella enterica* serovar Typhimurium *SpaPQR* operon with a C-terminal 3xFLAG tag on SpaR under the control of the *E. coli rhaB* promoter; *ori* cloDF13, Kan^r	[27]
pYT313	*sacB*-containing mobilizable suicide vector; Ap^r (Em^r)	[29]
pYT354	*sacB*-containing mobilizable suicide vector; Ap^r (Em^r)	[29]
pRHJ006	pETDuet-1 *porL*-(tev)-*gfp*-8xHis *porM*-twinstrep	This study
pRHJ007	pT12 *gldL gldM*(1-225)-twinstrep	This study
pRHJ008	pT12 *gldL gldM*(1-232)-twinstrep	This study
pRHJ011	Suicide plasmid used to delete *gldM*; 2.7-kbp upstream and 2.5-kbp downstream of *gldM* in pYT354	This study
pRHJ012	pGEM-T *gldL*	This study
pRHJ013	pGEM-T *gldM*	This study
pRHJ036	Suicide plasmid used to introduce the N10A codon change into *gldL*; *gldL(N10A)* in pYT354	This study
pRHJ037	Suicide plasmid used to introduce the Y13A codon change into *gldL*; *gldL(Y13A)* in pYT354	This study
pRHJ038	Suicide plasmid used to introduce the Y13F codon change into *gldL*; *gldL(Y13F)* in pYT354	This study
pRHJ039	Suicide plasmid used to introduce the K27A codon change into *gldL*; *gldL(K27A)* in pYT354	This study
pRHJ040	Suicide plasmid used to introduce the H30A codon change into *gldL*; *gldL(H30A)* in pYT354	This study
pRHJ041	Suicide plasmid used to introduce the S43A codon change into *gldL*; *gldL(S43A)* in pYT354	This study
pRHJ042	Suicide plasmid used to introduce the T48A codon change into *gldL*; *gldL(T48A)* in pYT354	This study
pRHJ043	Suicide plasmid used to introduce the E49A codon change into *gldL*; *gldL(E49A)* in pYT354	This study
pRHJ044	Suicide plasmid used to introduce the E49Q codon change into *gldL*; *gldL(E49Q)* in pYT354	This study
pRHJ045	Suicide plasmid used to introduce the E49D codon change into *gldL*; *gldL(E49D)* in pYT354	This study
pRHJ046	Suicide plasmid used to introduce the S56A codon change into *gldL*; *gldL(S56A)* in pYT354	This study
pRHJ047	Suicide plasmid used to introduce the R9A codon change into *gldM*; *gldM(R9A)* in pYT354	This study
pRHJ048	Suicide plasmid used to introduce the R9K codon change into *gldM*; *gldM(R9K)* in pYT354	This study
pRHJ049	Suicide plasmid used to introduce the R9E codon change into *gldM*; *gldM(R9E)* in pYT354	This study
pRHJ050	Suicide plasmid used to introduce the Q10A codon change into *gldM*; *gldM(Q10A)* in pYT354	This study
pRHJ051	Suicide plasmid used to introduce the K11A codon change into *gldM*; *gldM(K11A)* in pYT354	This study
pRHJ052	Suicide plasmid used to introduce the N14A codon change into *gldM*; *gldM(N14A)* in pYT354	This study
pRHJ053	Suicide plasmid used to introduce the Y17A codon change into *gldM*; *gldM(Y17A)* in pYT354	This study
pRHJ054	Suicide plasmid t used to introduce the Y17F codon change into *gldM*; *gldM(Y17F)* in pYT354	This study
pRHJ055	Suicide plasmid used to introduce the N27A codon change into *gldM*; *gldM(N27A)* in pYT354	This study
pRHJ058	Suicide plasmid used to introduce a Twin-Strep tag coding sequence to the end of *gldL*	This study
pRHJ059	Suicide plasmid used to construct the *gldL(N10A)-twinstrep* strain	This study
pRHJ060	Suicide plasmid used to construct the *gldL(Y13A)-twinstrep* strain	This study
pRHJ061	Suicide plasmid used to construct the *gldL(Y13F)-twinstrep* strain	This study
pRHJ062	Suicide plasmid used to construct the *gldL(K27A)-twinstrep* strain	This study
pRHJ063	Suicide plasmid used to construct the *gldL(H30A)-twinstrep* strain	This study
pRHJ064	Suicide plasmid used to construct the *gldL(S43A)-twinstrep* strain	This study
pRHJ065	Suicide plasmid used to construct the *gldL(T48A)-twinstrep* strain	This study
pRHJ066	Suicide plasmid used to construct the *gldL(E49A)-twinstrep* strain	This study
pRHJ067	Suicide plasmid used to construct the *gldL(E49Q)-twinstrep* strain	This study
pRHJ068	Suicide plasmid used to construct the *gldL(E49D)-twinstrep* strain	This study
pRHJ069	Suicide plasmid used to construct the *gldL(S56A)-twinstrep* strain	This study
pRHJ070	Suicide plasmid used to construct the *gldL-twinstrep gldM(R9A)* strain	This study
pRHJ071	Suicide plasmid used to construct the *gldL-twinstrep gldM(R9K)* strain	This study
pRHJ072	Suicide plasmid used to construct the *gldL-twinstrep gldM(R9E)* strain	This study
pRHJ073	Suicide plasmid used to construct the *gldL-twinstrep gldM(Q10A)* strain	This study
pRHJ074	Suicide plasmid used to construct the *gldL-twinstrep gldM(K11A)* strain	This study
pRHJ075	Suicide plasmid used to construct the *gldL-twinstrep gldM(N14A)* strain	This study
pRHJ076	Suicide plasmid used to construct the *gldL-twinstrep gldM(Y17A)* strain	This study
pRHJ077	Suicide plasmid used to construct the *gldL-twinstrep gldM(Y17F)* strain	This study
pRHJ078	Suicide plasmid used to construct the *gldL-twinstrep gldM(N27A)* strain	This study
pAK021	Suicide plasmid used to insert a HaloTag domain after the signal peptide of SprB	This study
pFL43	Expresses the cytoplasmic domain of GldL; pWALDO-sfGFPd *gldL(66-215)*	This study
pFL44	Expresses the periplasmic domain of GldM; pWALDO-sfGFPd *gldM(78-513)*	This study
pFL80	Suicide plasmid used to delete *porV*; 2.5-kbp upstream and 2.5-kbp downstream of *porV* in pYT313	[20]
pFL89	Suicide plasmid used to delete *gldL*; 2.6-kbp upstream and 2.5-kbp downstream of *gldL* in pYT313	This study
pPG01	Expresses the first 50 amino acids of RemA fused to mCherry and the C-terminal 97 amino acids of RemA; pCP-remA$_{us}$-mch-CTD97$_{remA}$	This study
pPG02	Expresses the first 50 amino acids of RemA fused to mCherry and the C-terminal 97 amino acids of RemA with the K1432A point mutation; pCP-remA$_{us}$-mch-CTD97(K1432A)$_{remA}$	This study

856

857 *Footnote:* [a] Selection markers functional in *F. johnsoniae* are in brackets

858

859   **Supplementary Data Table 1:** Oligonucleotides used in this study.

860

861   **Supplementary Data Video1:** Mutant strains gliding on glass. WT, *gldL$_{Y13A}$, gldL$_{Y13F}$, gldL$_{K27A}$, gldL$_{H30A}$,*

862   *gldL$_{E49D}$, gldM$_{R9K}$, gldM$_{Y17A}$* and *gldM$_{Y17F}$* cells are shown.

863   **Supplementary Data Video 2:** Fluorophore-labelled SprB adhesin moving on the surface of a WT cell.

864   **Supplementary Data Video 3:** Fluorophore-labelled SprB adhesin moving on the surface of a *gldL$_{Y13A}$*

865   cell.

866   **Supplementary Data Video 4:** Fluorophore-labelled SprB adhesin moving on the surface of a *gldL$_{K27A}$*

867   cell.

868   **Supplementary Data Video 5:** Fluorophore-labelled SprB adhesin moving on the surface of a *gldL$_{H30A}$*

869   cell.

870   **Supplementary Data Video 6:** Fluorophore-labelled SprB adhesin moving on the surface of a *gldM$_{R9K}$*

871   cell.

872   **Supplementary Data Video 7:** Fluorophore-labelled SprB adhesin moving on the surface of a -

873   *gldM$_{Y17F}$* cell.

874   **Supplementary Data Video 8:** Animation of a rotary model of GldLM function.

875